

# Dead zones as safe-havens for planetesimals: influence of disc mass and external magnetic field

Oliver Gressel<sup>1\*</sup>, Richard P. Nelson<sup>1\*</sup> and Neal J. Turner<sup>2\*</sup>

<sup>1</sup>*Astronomy Unit, Queen Mary University of London, Mile End Road, London E1 4NS*

<sup>2</sup>*Jet Propulsion Laboratory, California Institute of Technology, Pasadena, CA 91109, USA*

Accepted 1988 December 15. Received 1988 December 14; in original form 1988 October 11

## ABSTRACT

Planetesimals embedded in a protoplanetary disc are stirred by gravitational torques exerted by density fluctuations in the surrounding turbulence. In particular, planetesimals in a disc supporting fully developed magneto-rotational turbulence are readily excited to velocity dispersions above the threshold for catastrophic disruption, halting planet formation. We aim to examine the stirring of planetesimals lying instead in a magnetically-decoupled midplane dead zone, stirred only by spiral density waves propagating out of the disc’s magnetically-coupled turbulent surface layers. We extend previous studies to include a wider range of disc models, and explore the effects of varying the disc column density and external magnetic field strength. We measure the stochastic torques on swarms of test particles in 3D resistive-MHD stratified shearing-box calculations with ionisation by stellar X-rays, cosmic rays, and recombination on dust grains. The strength of the stirring is found to be independent of the gas surface density, which is contrary to the increase with disc mass expected from a simple linear wave picture. The discrepancy arises from the shearing out of density waves as they propagate into the dead zone, resulting in density structures near the midplane that exert weaker stochastic torques on average. We provide a simple analytic fit to our numerically obtained torque amplitudes that accounts for this effect. The stirring on the other hand depends sensitively on the net vertical magnetic flux, up to a saturation level above which magnetic forces dominate in the turbulent layers. For the majority of our models, the equilibrium planetesimal velocity dispersions lie between the thresholds for disrupting strong and weak aggregates, suggesting that collision outcomes will depend on material properties. However, discs with relatively weak magnetic fields yield reduced stirring, and their dead zones provide safe-havens even for the weakest planetesimals against collisional destruction.

**Key words:** accretion, accretion discs – MHD – methods: numerical – protoplanetary discs

## 1 INTRODUCTION

The formation of rocky earth-like planets, and the rock-ice cores of gas giant planets, are believed to involve assembly from a population of planetesimals that may range in size from 1 to 100 km. The existence of planets, asteroids and Kuiper-belt objects in our own solar system covering a wide-range in semimajor axes, in addition to the broad diversity in orbital properties of extrasolar planets (e.g. Mayor & Queloz 1995; Marois et al. 2010; Lissauer et al. 2011) and debris discs around main-sequence stars (Wyatt 2008), indicates that planetesimals form at orbital distances ranging from a few tenths of an au out to more than 100 au from the central star. While there remain many open questions about how planetesimals form within a protoplanetary disc, a number of plausible models

and scenarios have been suggested that exhibit differing degrees of sensitivity to the physical conditions within the disc.

Classical models of planetesimal formation (see e.g., Weidenschilling & Cuzzi 1993) involve an incremental process which starts from micron-sized dust grains. These grains grow via mutual collisions and sticking and settle toward the midplane of the protoplanetary disc (PPD). Assuming a laminar nebula a few times heavier than the minimum required to form the solar system (Hayashi 1981), Weidenschilling (2000) predicts a growth time scale equivalent to a few  $\times 10^4$  yr at 5 au. The main obstacle to the incremental formation scenario is the rapid inward migration of growing boulders once they reach sizes around one metre. Moreover, as demonstrated by Brauer et al. (2008), differential radial migration of a population of planetesimals of varying sizes can lead to high relative velocities implying collisional fragmentation.

In an attempt to avoid these difficulties, alternative formation scenarios have been proposed, which try to jump this metre-sized barrier by involving mechanisms of rapid planetesimal for-

\* E-mail: o.gressel@qmul.ac.uk (OG); r.p.nelson@qmul.ac.uk (RPN); neal.turner@jpl.nasa.gov (NJT)

mation. These alternative scenarios go back to the classic idea of Goldreich & Ward (1973), who proposed formation of planetesimals through gravitational instability in a dense layer of solids resulting from vertical settling of dust grains. Alternative scenarios that invoke rapid planetesimal formation include the concentration of mm-sized chondrules in turbulent eddies followed by direct gravitational collapse (Cuzzi et al. 2008), the streaming instability (Youdin & Goodman 2005), and particle trapping in zonal flows (Johansen et al. 2009). As demonstrated by Johansen et al. (2007, 2011), processes of this kind may ultimately lead to the rapid formation of bodies larger than Ceres via gravitational collapse of local concentrations of metre-sized objects, where the planetesimal masses depend on the disc mass.

Owing to their size, the emergence of planetesimals marks the transition into the gravitationally-dominated stage of planet formation. Runaway growth quickly leads to the formation of oligarchs (Wetherill & Stewart 1993; Kenyon & Bromley 2009), which subsequently grow into planetary embryos and cores via mutual collisions and accretion of smaller bodies (Ida & Makino 1993; Kokubo & Ida 1998). For this runaway growth to proceed efficiently, the velocity dispersion within the planetesimal swarm must remain significantly smaller than the surface-escape velocity of the accreting cores. Accounting only for self-stirring of the population, this is certainly expected in a fully laminar protostellar nebula. However, the explanation of the typical accretion rates of T Tauri stars requires an anomalous source of viscous redistribution of angular momentum, most likely explained by disc turbulence. This poses the question whether or not runaway growth remains a realistic proposition in a turbulent protoplanetary disc.

Planetesimals and protoplanetary embryos embedded in turbulent PPDs are subject to stochastic gravitational forces caused by density waves driven by the turbulent Maxwell stresses acting within the disc (Nelson & Papaloizou 2004). This issue was addressed in our previous work (Nelson & Gressel 2010, hereafter “Paper I”), where we compared global and local magneto-hydrodynamic (MHD) simulations of protoplanetary discs involving turbulence driven by the magneto-rotational instability (MRI, Balbus & Hawley 1991). Following the evolution of swarms of embedded test particles, we studied the effects of magnetic turbulence on the dispersion of planetesimal semimajor axes and the growth of their internal velocity dispersion. In agreement with an earlier study (Nelson 2005), we found that fully-developed disc turbulence at a level consistent with observational constraints (see e.g. Armitage 1998, and references therein) would cause large-scale diffusion of planetesimals over distances of several au (in contradiction of solar system constraints) and induce their collisional destruction.

However, as originally contemplated by Pneuman & Mitchell (1965), sustaining magnetic fields within the protosolar nebula requires the gas to be sufficiently ionised. This was later pointed out in the context of magnetised disc turbulence by Safronov (1972). In the wake of its discovery in the context of accretion discs, the linear development of the MRI was studied in detail for the case of ion-neutral drift (Blaes & Balbus 1994), and Ohmic diffusion (Jin 1996; Sano & Miyama 1999). The requirements for non-linear turbulence to be sustained have been studied by means of direct simulations for the case of Ohmic resistivity (Fleming et al. 2000), and ambipolar diffusion (Hawley & Stone 1998; Bai & Stone 2011). Because of the stabilising effect of epicyclic oscillations, a purely hydrodynamic flow is expected to be stable via the Rayleigh criterion (Rayleigh 1917). Lacking a plausible source for a sufficient number of free electrons, the flow is likely to remain in a laminar state.

Protoplanetary discs in the T Tauri stage are cold and dense, leading to the above mentioned low levels of ionisation (Umebayashi 1983). Based on the fact that the dominant ionisation sources are likely external to the disc itself, Gammie (1996) proposed a layered model for partially ionised accretion discs: While the disc surface layers are well ionised by stellar X-rays, and sustain a turbulent accretion flow caused by the MRI, the shielded disc interior is expected to harbour a ‘dead zone’ where the flow remains laminar implying negligible levels of accretion. Such layered discs were first investigated numerically by Fleming & Stone (2003), who included a magnetic diffusivity varying with height. Their box simulations demonstrated that the flow within the dead zone-region maintains a modest Reynolds stress due to waves being excited by the active layers.

Owing to the high gas density in the bulk of the disc and the embedded sub-micron dust grains, a number of physical effects may significantly affect the overall ionisation balance. This holds true for both PPDs in general, and the protosolar nebula in particular (Hayashi 1981). The effect of dust on charge carriers was first investigated by Sano et al. (2000). In a series of papers, Ilgner & Nelson studied the effect of small dust grains and different chemical reaction networks (Ilgner & Nelson 2006a), and the role of turbulent mixing (Ilgner & Nelson 2006b). An additional complication arises when one considers the Hall term in Ohm’s law (Wardle 1999), introducing a dichotomy with respect to the mutual orientation of any vertical magnetic flux and the rotation axis (Wardle & Salmeron 2011). A study of the effect of the Hall term on the MRI turbulence saturation amplitude by Sano & Stone (2002) found it to be little changed for the range of Hall parameters they investigated.

Studies of the effects of ohmic dissipation determined by time-dependent reaction networks coupled to the MHD evolution have been presented by Turner et al. (2007) and Ilgner & Nelson (2008). These works have shown that enlivening the dead zone via turbulent mixing of charge carriers is only efficient in the absence of small dust grains. However, if a significant population of micron sized grains is present, the adsorption time scale of free electrons is short enough to maintain the dead zone (Turner & Sano 2008; Bai 2011). Inutsuka & Sano (2005) have suggested that fast moving electrons generated in magnetic reconnection events may provide a source of ionisation that can remove or modify the dead zone, but detailed calculations demonstrating the feasibility of this idea have yet to be done.

Building on this line of work, we have extended our study from Paper I to the case of stratified PPDs. This includes a fiducial model being fully MRI active, and two models including a magnetically inactive midplane region (Gressel, Nelson & Turner 2011, hereafter “Paper II”). The key results of this study were that the stirring of the planetesimals’ velocity dispersion was much reduced in the dead zone, as was their radial diffusion – satisfying the observational constraint that radial mixing of asteroids has probably not occurred over distances  $\gtrsim 0.5$  au (Gradie & Tedesco 1982).

This possibly allows for the continued growth of planetesimals rather than destruction or erosion during collisions, and it was suggested that dead zones may provide safe havens for planetesimals. One perceived limitation of Paper II was that we restricted ourselves to the case of a minimum mass protosolar nebula. While one would expect the strength of the stirring to scale approximately linearly with the disc mass (all other things being equal), the relative level of density fluctuations might be affected by the extended width of the dead zone. It is the purpose of this paper, to elucidate on the net effect of these two counteracting dependencies, and

**Table 1.** Overview of simulation parameters, including model D1 from Paper II. The fiducial model D1.1 is identical to D1 and serves as a control for the changes described in Sect. 2.3 below.

	$\rho_{\text{mid}}$	$\Sigma$ [ $\frac{\text{g}}{\text{cm}^2}$ ]	domain [ $H$ ]	resolution
D1 / D1.1	1	134.6	$3 \times 12, \pm 5.500$	$72 \times 144 \times 264$
D1.2	2	269.2	$3 \times 12, \pm 5.667$	$72 \times 144 \times 272$
D1.4	4	538.4	$3 \times 12, \pm 5.833$	$72 \times 144 \times 280$

moreover to examine the influence of varying the imposed magnetic field strength.

This paper is organised as follows: the physical model and numerical methods are briefly recapitulated in Section 2; for a more thorough description, we refer the reader to Paper II. Simulation results are presented in three parts: in Section 3 we study the dependence on the disc mass/column density, and in Section 4, we show results on the variation with the external magnetic field permeating the disc vertically. A modified scaling relation to encompass all the obtained results is then developed in Section 5. Implications for the scope and applicability of our results for planet formation theory are discussed in Section 6, and conclusions are drawn in Section 7.

## 2 METHODS

The simulations presented in this paper are based on our fiducial dead zone model D1 discussed in Paper II. We again solve the standard equations of resistive MHD in a locally corotating, Cartesian coordinate frame ( $\hat{x}, \hat{y}, \hat{z}$ ), adopting the shearing box formalism (see Gressel & Ziegler 2007, and eqns. in sect. 2 of Paper II). Embedded in the dynamically evolving plasma are swarms of 25 non-interacting massive test particles, which are affected by disc gravity and the inertial forces in the local frame of reference. All simulations utilise the NIRVANA-III code (Ziegler 2004); further modifications to the solver are documented in sect. 2.4 of Paper II.

The base state of our model is given by isothermal stratification in a fixed gravitational potential  $\Phi(z)$ . Unlike in earlier studies (Fleming & Stone 2003; Oishi et al. 2007), and to allow for sufficiently wide MRI-active regions, model D1 used a box size of 5.5 scale heights,  $H$ , on each side of the disc midplane.<sup>1</sup> Based on our previous analysis of the influence of box size on gravitational stirring (Paper I), we furthermore maintain a horizontal box size of  $3 \times 12 H$ , permitting the excitation of spiral density (SD) waves (Heinemann & Papaloizou 2009a,b, 2011).

Because the resistivity  $\eta$  depends on a physically motivated ionisation model involving chemical rate equations, we have to introduce a unit system to convert code units into standard units. To maintain continuity with Paper II, we adopt the same basic disc model, which is similar to the widely used “minimum-mass” protosolar nebula (Hayashi 1981). At 5 au the Hayashi model has a column density  $\Sigma = 150 \text{ g cm}^{-2}$  and a disc opening angle  $H/r = 0.047$ . We adopt similar values  $\Sigma = 135 \text{ g cm}^{-2}$  and  $H/r = 0.05$ , giving a temperature  $T = 108 \text{ K}$ , and an isothermal sound speed of  $c_s = 667 \text{ m s}^{-1}$  (also cf. Tab. 2). Because the minimum-mass assumption does in fact only specify a lower limit to the expected

<sup>1</sup> With our definition of  $H$ , the equilibrium density profile is proportional to  $\exp(-z^2/(2H^2))$ , i.e.  $H$  is identical to the ‘ $h$ ’ in Okuzumi & Hirose (2011).

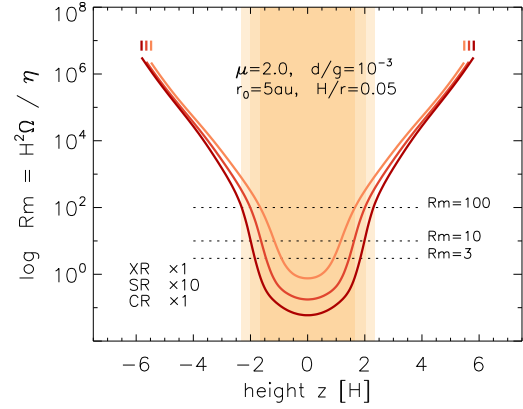


**Figure 1.** Vertical  $\eta$  profiles for the runs presented in this paper. We plot the magnetic Reynolds number,  $\text{Rm} = \Omega H^2 \eta(z)^{-1}$  determined from our ionisation model. The three lines represent the initial models for runs D1, D1.2, and D1.4, respectively (cf. Tab. 1); short vertical bars illustrate the varying domain size  $L_z$ .

**Table 2.** List of model parameters. Note also that magnetic field values for each run are listed in the third column of table 3.

parameter	symbol	value	unit
orbital location	$a$	5.0	au
disc aspect ratio	$h$	0.05	
local temperature	$T$	108	K
mean molecular weight	$\bar{\mu}$	2.0	amu
gas/dust ratio		0.001	
dust particle size		0.1	$\mu\text{m}$
dust grain density	$\rho_d$	3.0	$\text{g cm}^{-3}$
disc column density	$\Sigma$	135 – 538	$\text{g cm}^{-2}$
magnetic field strength	$\bar{B}_z$	2.68 – 43	mG

mass of the protosolar nebula at the age when planetesimal formation likely occurred, we here study further models with double and four-times the midplane density  $\rho_{\text{mid}}$  (see Tab. 1). The ionisation fluxes for X-rays (XR), short-lived radionuclides (SR), and cosmic rays (CR) are unchanged from model D1, i.e., XR and CR fluxes are the nominal values, and SRs are enhanced by a factor of ten; see Sect. 2.2.1 for further details. For studying the influence of the net vertical field (NVF), we performed additional runs D1-WF (with a weak field), D1-NVF a/b (with varying field), and two extra models based on D1.4 with weaker fields. We adopt a standard resolution of 24 grid cells per  $H$  in the radial, and vertical directions; for the azimuthal direction we use a reduced grid spacing of  $12/H$ . A basic convergence check is provided in Appendix A.

### 2.1 Initial and boundary conditions

A primary aim of this work is to construct discs of varying mass in which the active zone remains essentially unchanged in its mass and level of turbulence in each model, with the only change being in the mass and vertical thickness of the dead zone. This component of our study then becomes one in which we examine the effect of varying the mass of the dead zone keeping all other parameters fixed (see Tab. 2 for reference). The numerical set-up we adopt for the models of varying disc mass is designed to achieve this aim.

The initial magnetic field is a superposition of two components, a standard zero-net-flux (ZNF) configuration  $B_z(x) \sim$

$\sin(2\pi x/L_x)$ , and a weak additional vertical net-flux (NVF) component representing an external or dynamo-generated field. We vary the strength of the initial ZNF flux to produce a plasma parameter (i.e. the ratio of thermal to magnetic pressure)  $\beta_p \approx 50$  independent of the midplane density (and hence pressure) of the three studied models. In contrast, we keep the absolute strength of the external net vertical flux (which is conserved during the simulations) fixed at a value corresponding to  $B_0 = 10.73$  mG in physical units, resulting in a weaker relative field in the midplane of models with higher mass loading. Note that the NVF component leads to a plasma parameter varying with height. As a consequence, the region of intermediate field strength, i.e. the vertical range, where the most unstable nonaxisymmetric MRI modes fit into the box, moves up in the disc. We expect the resulting active regions to be of similar vertical extent irrespective of the mass loading, but separated by a wider dead zone in the case of heavier discs as is illustrated by shaded areas in Fig. 1. To maintain near-identical active zones across all runs, we adjust the vertical box size accordingly (cf. Tab. 1).

The simulations that examine the influence of varying the strength of the net vertical magnetic field strength (models D1-NVFa and D1-NVFB) are initiated with specific values of the magnetic field ( $B_0 = 2.68$  mG and  $B_0 = 10.73$  mG, respectively), and after every 40 orbits the field strength is incremented by factors of two up to some maximum value. Although we only adopt two run labels for these simulations, these simulations in fact explore the influence of six different external magnetic field strengths ranging between 2.68 mG and 86 mG.

As discussed in more detail in Paper II, for the fluid variables, we use vertical boundary conditions allowing material to leave the box but prevent inflow. Mass loss associated with the outflow boundaries is compensated by continually re-instating the initial density profile in each grid cell by means of an artificial mass source term (cf. Hanasz et al. 2009). Because of the low density in the halo, the relative change in the disc mass due to outflow is very low (on the order of  $10^{-4}$  per orbit). We have verified that the additional term does not affect the obtained stirring amplitudes. As in our previous work, we compute a locally and temporally varying magnetic diffusivity  $\eta(\mathbf{x}, t)$ . This adds to the level of realism achieved in earlier simulations of dead zones by Fleming & Stone (2003) and Oishi et al. (2007), who used static diffusivity profiles. Here we briefly re-capitulate the physical ionisation model we implement and refer the reader to section 2.3 of Paper II for a more detailed discussion.

## 2.2 The diffusivity model

Because of the expected dominance of small dust grains (Sano et al. 2000; Ilgner & Nelson 2006a), we decide to avoid following the detailed non-equilibrium chemistry and adopt a simplified approach for the gas-phase reactions. Assuming that recombination happens much faster than any dynamical mixing timescale in our system, we update  $\eta$  according to a precomputed table derived from the reaction network in mode14 of Ilgner & Nelson (2006a). When computing the resistivity, we include the contributions of all the charged species following Wardle (2007), eqns. (21)-(31). For the free parameters, we assume the same values described in Paper II, i.e. dust grains of size  $0.1\mu\text{m}$  and with density  $3\text{ g cm}^{-3}$  and a dust-to-gas mass ratio of  $10^{-3}$  (such that we tacitly assume that 90 percent of the solid grains have already grown to become larger bodies). The gas-phase abundance of Magnesium is taken to be depleted by a factor  $10^{-4}$  compared to its solar value (with the remainder assumed to be bound-up in grains). The key factor governing the

diffusivity  $\eta$ , is the local ionisation rate  $\zeta(\mathbf{x}, t)$ , which is computed from the external irradiation by evaluating column densities to both the upper and lower disc surfaces. Because of the expected radial density features, related to the excited spiral waves, this is done on a per-grid-cell basis.

### 2.2.1 Ionisation sources

The ionisation model is founded on the work of Turner & Drake (2009), who studied how stellar X-rays, radionuclides, and energetic protons can influence the shape and extent of a possible dead zone via their effect on Ohmic diffusion. Implementing the model of Turner & Drake (2009), we focus on stellar X-rays (XR), and interstellar cosmic rays (CRs) as the prime sources of ionisation. As a representative value, we chose  $L_{\text{XR}} \approx 2 \times 10^{30}$  erg  $\text{s}^{-1}$  as suggested by Garmire et al. (2000). Applying a simple fit to the Monte-Carlo radiative transfer calculations of Igea & Glassgold (1999), we approximate the ionisation rate due to X-rays by

$$\zeta_{\text{XR}} = 2.6 \times 10^{-15} \text{ s}^{-1} \left[ e^{-\Sigma_a/\Sigma_{\text{XR}}} + e^{-\Sigma_b/\Sigma_{\text{XR}}} \right] r_{\text{au}}^{-2}, \quad (1)$$

with  $\Sigma_a$  and  $\Sigma_b$  the gas column densities above and below a given point, and  $\Sigma_{\text{XR}} = 8.0 \text{ g cm}^{-2}$  the assumed X-ray absorption depth. For the vertical attenuation of interstellar CRs illuminating the disc surfaces, we adopt the formula given in Umebayashi & Nakano (2009):

$$\zeta_{\text{CR}} = 5 \times 10^{-18} \text{ s}^{-1} e^{-\Sigma_a/\Sigma_{\text{CR}}} \left[ 1 + \left( \frac{\Sigma_a}{\Sigma_{\text{CR}}} \right)^{\frac{3}{4}} \right]^{\frac{4}{3}} + \dots, \quad (2)$$

where  $\Sigma_{\text{CR}} = 96 \text{ g cm}^{-2}$  is the cosmic ray attenuation depth (Umebayashi & Nakano 1981), and dots indicate the corresponding contribution from the second column density  $\Sigma_b$ . We further include an ambient ionisation due to the decay of short-lived radionuclides (SR). As already done for model D1, and to somewhat limit the dynamic range in  $\eta$ , the related ionisation is chosen  $10\times$  the nominal value of  $\zeta_{\text{SR}} = 3.7 \times 10^{-19} \text{ s}^{-1}$  quoted in Turner & Drake (2009).

## 2.3 The induction equation

When simulating protoplanetary discs with dead zones using the shearing box approximation, there are two issues that arise which must be addressed to increase the feasibility and realism of the models. The first occurs because we are solving an advection-diffusion equation in time-explicit fashion. The time step size is restricted by the time for diffusion across one grid cell, and because this quantity scales with the square of the grid spacing, the presence of large diffusion coefficients can render the computational effort prohibitive in highly resolved runs. This was addressed in our previous paper by limiting the dynamic range in  $\eta$  and applying the technique of temporal sub-cycling to the diffusive part of the induction equation (cf. sect. 2.3.2 in Paper II). With the more extended dead zones of models D1.2 and D1.4, the time scales become even more disparate, and we have developed a modified scheme to deal with this, described in detail in Appendix B.

The second issue relates to the generation of strong azimuthal magnetic fields through the winding up of net radial fields in the box. Although our simulations begin with zero net radial magnetic field in the computational domain, advection of horizontal field components through the open vertical boundary leads to the generation of net radial fields that may diffuse into the dead zone. Once there, Keplerian shear may wind them up to generate strong azimuthal fields that subsequently leak back into the active regions,

modifying the turbulence there. This issue has been discussed by Turner & Sano (2008), where it was noted that the winding of fields generates a strong radial gradient in the azimuthal field strength due to the Keplerian rotation profile in global discs, leading to radial diffusion of the strong fields that limits their growth. This radial diffusion cannot occur in a shearing box due to the uniform shear and periodic boundary conditions (but has been observed in the global simulations presented by Dzyurkevich et al. (2010)), so we have developed an approximate scheme designed to crudely mimic the radial diffusion of fields in global discs. We refer to this scheme as super-box scale diffusion, and we describe its implementation in Appendix B.

### 3 DEPENDENCE ON DISC MASS

In Paper II, we restricted our analysis to the fiducial case of a minimum mass protosolar nebula, and this naturally begs the question how the results will be affected if one looks at more massive discs. A major aim of this study is to compute disc models with different masses/surface densities that have very similar active layers in terms of mass and turbulent activity. The main difference between the models will then be the physical depth and mass of the dead zone. Density waves that are excited in the active layer will propagate into the dead zone and induce gravitational stirring of the planetesimals there through the density fluctuations that they generate. A key question is how this stirring depends on disc mass.

#### 3.1 Scaling relations for linear density waves

Based on the results of simulations presented in paper II, we expect the disc models described below to have the following midplane-symmetric three-layer structure: a non-turbulent dead zone located at and above the midplane in which the MRI is quenched by Ohmic resistivity, on top of which lies a turbulent region in which the MRI operates unaffected by resistivity. At disc altitudes above the MRI-active region lies a magnetically dominated halo in which the field strength is too large for the MRI to operate because unstable modes do not fit within the available vertical extent. Density waves excited at the interface between the dead zone and MRI-active layer will propagate into the dead zone, creating density fluctuations at the midplane.

We denote the density at the active/dead zone interface as  $\rho_{\text{int}}$ . The disc models of different mass we compute are designed to generate discs in which very similar active layers lie above and below dead zones of different mass, and for which the midplane density,  $\rho_{\text{mid}}$ , scales with the disc mass. We expect each of our models therefore to have very similar values of the density,  $\rho_{\text{int}}$ , and perturbed velocity,  $\delta v_{\text{int}}$ , at the dead/active zone interface. Linear density waves that travel sonically into the dead zone should conserve energy as they propagate, such that we expect  $\rho_{\text{mid}}(\delta v_{\text{mid}})^2 \simeq \rho_{\text{int}}(\delta v_{\text{int}})^2$ , where  $\delta v_{\text{mid}}$  is the perturbed velocity at the midplane. Relative density fluctuations for isothermal sound waves satisfy the relation

$$\frac{\delta\rho}{\rho} = \frac{\delta v}{c_s} \quad (3)$$

such that relative density fluctuations at the disc midplane should obey the scaling

$$\left(\frac{\delta\rho}{\rho}\right)_{\text{mid}} \propto \frac{1}{\sqrt{\rho_{\text{mid}}}}. \quad (4)$$

Translated into absolute density fluctuations, this implies a scaling  $\delta\rho_{\text{mid}} \propto \sqrt{\rho_{\text{mid}}}$ . It is reasonable to expect the fluctuating torque,  $\Gamma_y$ , induced by density fluctuations near the midplane will scale linearly with  $\delta\rho_{\text{mid}}$ , leading to the naive expectation that stochastic torques will scale according to  $\Gamma_y \propto \sqrt{\rho_{\text{mid}}}$ .

At the time of writing an extensive study of MRI turbulence in layered accretion discs appeared in print (Okuzumi & Hirose 2011). For a broader discussion about scaling relations in disc models with dead zones we refer the reader to this recent publication.

#### 3.2 Disc evolution

As in sect. 3.2 of Paper II, we will start our discussion by looking at the evolution of the gas disc as shown in Figure 2. Owing to the additional magnetic diffusion term (cf. Sect. B2), the overall evolution of model D1.1 (left hand panels) appears somewhat less intermittent than the identical setup from model D1 in Paper II. This is also true for the heavier models D1.2 (centre) and D1.4 (right hand panels).

The different models in fact appear very similar, e.g., in terms of the cycle frequency of the field reversals and the overall field amplitude. Also the stresses and relative density fluctuations within the MRI-active regions are nearly identical. The only apparent trend is seen in the relative density fluctuations in the midplane region, which fall off with mass loading. The relative amplitudes, as listed in column 7 of Tab. 3, are 0.091, 0.058, and 0.038, respectively, which implies a scaling with the midplane density to the power of  $\sim -0.63 \pm 0.01$ ; this is in decent agreement with the expected scaling  $(\delta\rho_{\text{mid}}/\rho_{\text{mid}}) \propto \rho_{\text{mid}}^{-1/2}$  discussed above in Sect. 3.1. The discrepancy can partly be ascribed to the varying  $\delta\rho|_{\Lambda=1}$  at the layer interface (cf. Sect. 3.3 below), which shows a slight trend – with a power  $\sim -0.05 \pm 0.01$  – towards weaker absolute fluctuations in heavier discs. Overall, the results indicate that the propagation of density waves from the transition region between the active and dead zones occurs without significant dissipation of energy.

Because our model assumes that the main source of ionisation is exterior to the disc surface, the width of the dead zone depends on the column density of the shielding material. The extent of the dead zone as a function of various ionisation sources was studied in detail by Turner & Drake (2009). In our simulations, we determine the transition region via the criterion that the Elsasser<sup>2</sup> number  $\Lambda \equiv v_A^2/(\Omega\eta)$  equals unity (indicated by a solid black line in Fig. 2). This yields a time-averaged half thickness of  $1.66 \pm 0.04$ ,  $2.02 \pm 0.03$ , and  $2.33 \pm 0.03 H$  for models D1.1-4, respectively. In other words, doubling the disc mass increases the extent of the dead zone by a third of a pressure scale height  $H$ . As can be seen from Fig. 2, the extent of the different layers is remarkably stationary. As a result, the dead zone thickness only fluctuates on the per-cent level. This has, of course, to be taken with a grain of salt. External conditions (e.g., gas inflow from the parent molecular cloud, stellar X-ray luminosity, intensity of arriving CRs, ...) in a realistic protoplanetary disc are likely to vary strongly both in time and space. However, the relative quiescence of our experimental setup will allow us to quantify the secular evolution of the embedded planetesimals more accurately.

<sup>2</sup> We note, in passing, that this definition is formally identical to what has been called a Lundquist number (or even magnetic Reynolds number) in related publications. Irrespective of its name,  $\Lambda < 1$  serves as a robust indicator for suppression of the fastest-growing MRI mode (see Pessah 2010).

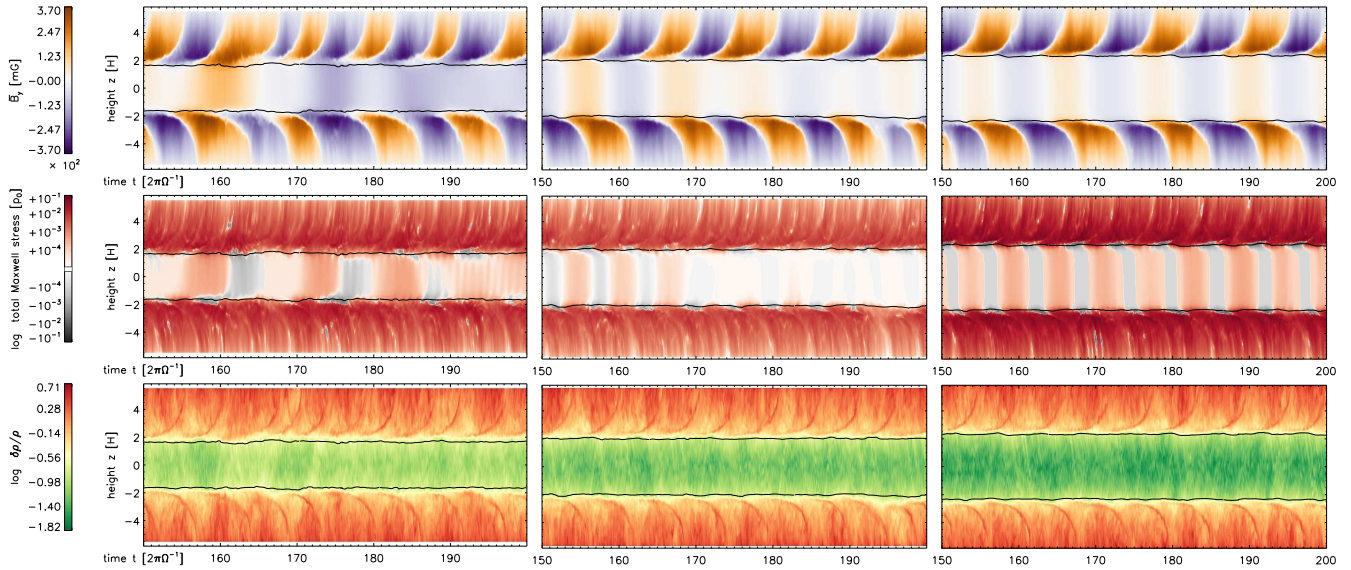


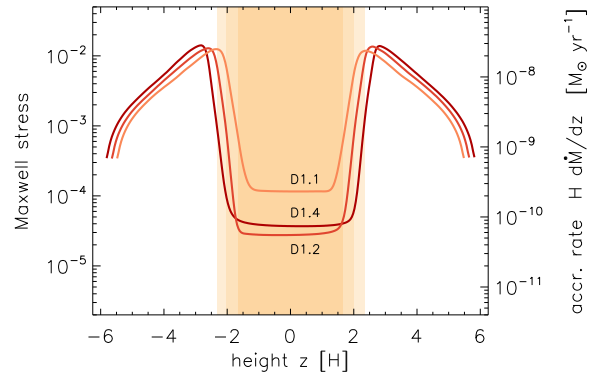
**Figure 2.** Space-time evolution of the mean toroidal field  $\bar{B}_\phi$  (upper row), total Maxwell stress  $M_{r\phi} = -\langle B_R B_\phi \rangle$  (middle row), and relative density fluctuation  $\delta\rho/\rho$ , (bottom row). The different panels show runs D1.1 (left), D1.2 (centre), and D1.4 (right). The interface between the live and dead zones is indicated by a solid line representing the criterion  $\Lambda \equiv v_A^2/(\Omega\eta) = 1$ . Note the trends of a wider dead zone, and weaker *relative* density perturbations when going to higher densities, while most disc properties remain virtually unchanged.

### 3.3 Disc vertical structure

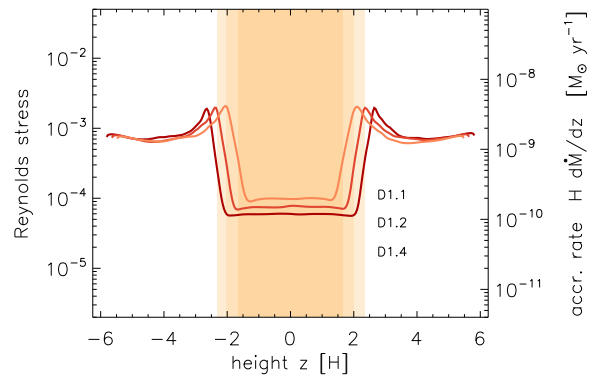
Having assured ourselves of the stationary nature of the flow, we can now proceed and look at the characteristic structure of the layered disc. In Figure 3, we plot the time-averaged (20–220 orbits) Maxwell stress  $M_{r\phi} = -\langle B_R B_\phi \rangle$  for the three models D1.1–4, of varying column density. As discussed in the last section, owing to the random diffusion of flux into the midplane region, there is no systematic to the residual level within the dead zone. As noted earlier, we expect the MRI-active zone to move away from the midplane for the higher density models, and this trend is clearly seen. As a result, we infer very similar vertically-integrated mass accretion rates of  $7.90 \times 10^{-8}$ ,  $7.97 \times 10^{-8}$ , and  $7.86 \times 10^{-8} M_\odot \text{ yr}^{-1}$  for runs D1.1–4, respectively. This is in-line with the volume-averaged values stated in column 4 of Tab. 3 and demonstrates that higher mass loading does not affect the level of activity or mass in the active zone, but merely the vertical extent and mass of the dead zone, such that the nonlinear evolution of the disc models arising from the specified initial conditions is as intended.

Figure 4 shows the same shift away from the midplane for higher disc mass in the hydrodynamic stresses  $\langle \rho v_r \delta v_\phi \rangle$ . The associated, vertically integrated mass accretion rates are  $1.28 \times 10^{-8}$ ,  $1.33 \times 10^{-8}$ , and  $1.41 \times 10^{-8} M_\odot \text{ yr}^{-1}$  for models D1.1–4, respectively, i.e. the bulk of the transport is due to magnetic stresses. Within the dead zone, the Reynolds stresses scale with the gas density but this trend is very weak at their respective peak position, which lies just outside the layer interface. This region is of particular interest as it marks the position in the disc where the turbulent fluctuations created by the MRI-active layers are most energetic in terms of their mass loading and hence their associated momenta. Tracing the interface via the  $\Lambda = 1$  criterion, we obtain very similar *absolute* density fluctuations at this line. The respective values are  $\delta\rho|_{\Lambda=1} = 0.045$ ,  $0.043$ , and  $0.042$  for models D1.1–4

We conclude that, in all three models, the dead zone sees a very similar boundary separating it from the active zone, with the only difference being in its physical separation from the particle swarm located near  $z = 0$ . In the following section, we will deter-



**Figure 3.** Time-integrated Maxwell stresses for models D1.1–4 as labelled. The vertical displacement of the curves demonstrates nicely why all models produce the same mass accretion rate. Shaded areas indicate the extent of the dead zone in each model.



**Figure 4.** Time-integrated Reynolds stresses for models D1.1–4. The same vertical displacement as in Fig. 3 is seen. The peaks in the stress sits just outside the transition region between the active and inactive layers (shaded).

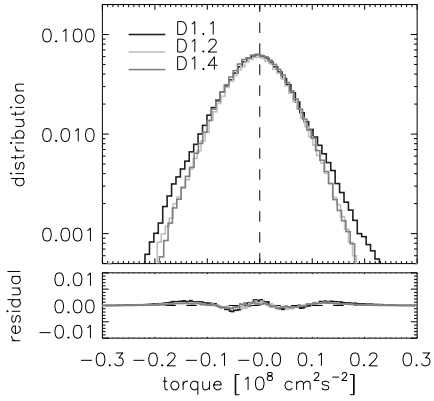


**Figure 5.** Torque distributions  $\Gamma_y$  for the models D1.1-4 with varying disc mass. Residuals indicate the deviation from a normal distribution.

mine the consequences this has on the gravitational forcing exerted onto the planetesimals, and examine if the stochastic torques follow the scaling predicted in Sect. 3.1.

### 3.4 Gravitational torques

It was established in the global simulations of Nelson & Papaloizou (2004) and Nelson (2005) that density fluctuations from developed turbulence lead to stochastic gravitational forces which can have a significant impact on the dynamical evolution of embedded planetesimals and protoplanets. We remark that earlier shearing box simulations of MHD turbulence have shown the development of axisymmetric pressure bumps or ‘zonal flows’ (Johansen et al. 2009), which may influence the stirring of planetesimals. Analysis of our simulation D1.1 suggests that the midplane density supports a long-lived (20-30 orbits), axisymmetric density asymmetry across the radial width of the box with amplitude  $\sim 1\%$ . This may be an indication that weak zonal flows arise even in the presence of a dead zone. The role of this in stirring planetesimals is unclear at present and will be the subject of a future study.

In our previous papers, we have quantified the level of stirring for a range of disc models. We here perform a similar analysis and find broad agreement with previous runs. In particular, model D1.1 agrees well with the earlier run D1 from Paper II – we attribute the discrepancy of about ten per-cent in the torques between D1 (0.06) and D1.1 (0.054) to the lower level of sampling noise achieved in the new set of simulations, where a more conservative choice for the gravitational softening parameter was taken. We note that when statistically<sup>3</sup> correcting the original results from D1 for a weak systematic dependence on the particle position on the grid, excellent agreement can be obtained.

#### 3.4.1 Torque distribution functions

Torque time series,  $\Gamma_y(t)$ , are derived from the gravitational forces acting on the particles along the  $y$  direction within our simulation box, and are recorded along the evolving trajectory of the particles. Torque amplitudes,  $\sigma(\Gamma_y)$ , for the different runs are obtained from a Gaussian fit to the histograms as depicted in Figure 5. Averaging over the swarm of 25 particles and sub-intervals in time

<sup>3</sup> As different locations ought to be indiscriminate in a stochastic sense, this is done by binning the full data with respect to particle position (at sub-grid resolution) and then removing the median torque for each bin.

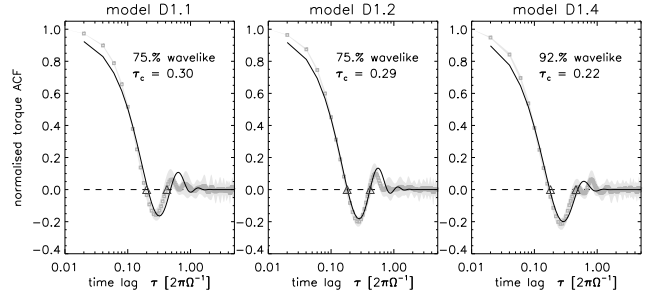


**Figure 6.** Autocorrelation functions (ACFs) of the torque time series, averaged over 25 particles, and 4 sub-intervals in time (shaded areas). The first and second zero crossing are indicated by a triangle. Labels give the fitted coherence time along with the relative amplitude of the wavelike feature.

allows us to estimate error bars, and we infer values of  $\sigma(\Gamma_y) = 0.054 \pm 0.004$  for model D1.1, and  $0.052 \pm 0.003$  for both models D1.2 and D1.4 (these values are also listed for reference in column eight of Table 3). This demonstrates that the width of the torque distribution is remarkably insensitive to the column density, and models D1.1 through D1.4 agree to within five per-cent, which is somewhat smaller than the error bars. This result is in clear conflict with the simple scaling law based on conservation of wave energy for isothermal sounds waves (see Sect. 3.1).

Naive expectations suggest that fluctuating torques experienced by solid bodies located near the disc midplane will scale linearly with absolute density fluctuations there, where we both predict and observe the scaling  $\delta\rho_{\text{mid}} \propto \sqrt{\rho_{\text{mid}}}$ . Thus, we expect the fluctuating torque amplitude to scale with the square-root of the disc mass in these simulations. As discussed in Sect. 3.3, we find that all models agree on the relative density fluctuations at the transition between the dead and active zone, and the absolute and relative density fluctuations at the midplane are in good agreement with the scaling arguments (also cf. Fig. 13). This suggests that a more subtle effect is responsible for modifying the expected linear scaling between the midplane density fluctuations,  $\delta\rho_{\text{mid}}$ , and the rms torque fluctuations,  $\sigma(\Gamma_y)$ , shown in Figure 5. A factor of four change in disc mass between models D1.1 and D1.4 should lead to a factor of two change in the torque amplitude, and this would clearly be detectable if present. We defer a more detailed discussion of this issue until Sect. 5, where we provide evidence to resolve the discrepancy between the simulation results and linear scaling.

#### 3.4.2 Torque autocorrelation

How does the modified amplitude of the density waves influence the temporal coherence of the stochastic torques? We recall from our previous work that the torque autocorrelation function (ACF) appeared as a superposition of a truly stochastic part and a modulated ‘‘wavelike’’ feature (due to the quasi-periodic passage of density waves through the particle’s location). This dual character, which is also seen in the corresponding figs. 9 and 15 of Oishi et al. (2007) and Yang et al. (2009), was described in terms of a formula which we introduced in section 3.3 of Paper I:

$$S_T(\tau) = [(1 - a) + a \cos(2\pi \omega \tau)] e^{-\tau/\tau_c}. \quad (5)$$

Fitting parameters are the relative amplitude  $a$ , the frequency of the wavelike modulation  $\omega$ , and the coherence time  $\tau_c$  of the stochastic envelope. The resulting fits for the models D1.1-4 are plotted in Fig. 6, where we also state the obtained values for the relevant fitting parameters. In terms of the parameter of primary interest, the

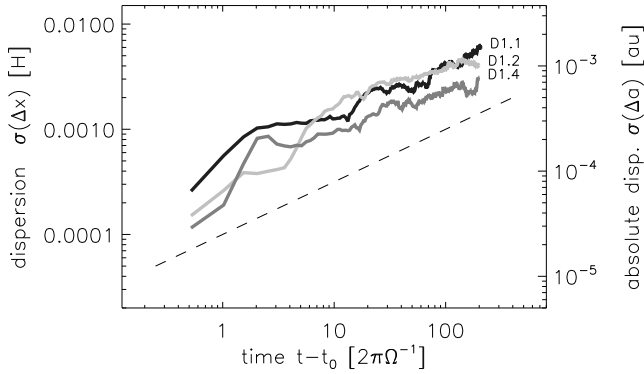


**Figure 7.** Random-walk behaviour for the rms radial displacement  $\sigma(\Delta x)$ . The right hand axis shows the absolute dispersion  $\sigma(\Delta a)$  at  $a_0 = 5$  au. Note that model D1.4 appears to show a slightly reduced tendency for particle dispersion.

coherence time  $\tau_c$ , models D1.1 and D1.2 show excellent agreement with model D1 from Paper II. Note that while model D1 showed a  $\sim 55\%$  wavelike modulation, this is now increased to  $\sim 75\%$ . We believe that this relative increase in the wave feature is, in fact, a reduction of the stochastic component caused by the lower level of random sampling noise in the new set of simulations. When correcting for this in model D1, we also obtain a wavelike amplitude of  $\sim 75\%$ . The modulation is even more pronounced in model D1.4, which moreover shows a significantly reduced coherence time of  $\tau_c = 0.22$ . One can see by inspection of the over-plotted model curves that there exists some tension between our simplistic approach and the actual data. We conclude that a more accurate determination will require a more thorough understanding of the ACF shape. Yet, ultimately the derived stochastic description via  $\sigma(\Gamma_y)$  and  $\tau_c$  can be verified by comparison with the amount of particle diffusion present in the simulations, as we shall demonstrate in the next section.

### 3.5 Radial diffusion of planetesimals

Having demonstrated that the gravitational torques acting on embedded planetesimals can be approximated by a normal distribution, and their temporal correlations possess a finite coherence time, we can now exploit these two properties to predict the amount of particle diffusion based on a Fokker-Planck-type model. This approach was described in detail in section 6 of Paper II, and we here briefly recapitulate the essential ingredients. Particle spreading occurs because stochastic torques cause diffusion of planetesimal angular momenta at a rate given by the diffusion coefficient  $D_p = \sigma(\Gamma_y)^2 \tau_c$ . This leads to an estimated spread in semi-major axis  $a$  after an evolution time,  $t$ , of

$$\Delta a = \frac{2a_0 \sqrt{D_p t}}{\sqrt{GM a_0}}, \quad (6)$$

as was derived in eqns. (16)-(19) in Paper II. This estimate for  $\Delta a$  can then be confronted with a random walk-type fit to the rms particle displacement in semimajor axis due to diffusion,  $\sigma(\Delta x)$ , obtained in the simulations

$$\frac{\sigma(\Delta x)}{H} = C_\sigma(\Delta x) \sqrt{t}, \quad (7)$$

corresponding to eqn. (20) in Paper II. The rms spread in the local displacement  $\Delta x \equiv \Delta(a - a_0)$  is plotted in Fig. 7 for the different models. Owing to the relatively small number of particles, the

curves display substantial random fluctuations, yet the general behaviour of a random walk-like growth emerges, and it can further be seen that the rate of planetesimal spreading in the runs is similar, as expected from the earlier discussion concerning the similarity of the stochastic torques in the three runs. The fitted values obtained for  $C_\sigma(\Delta x)$  are  $(4.56 \pm 0.54) \times 10^{-4}$  for model D1.1, and  $(4.36 \pm 0.32) \times 10^{-4}$  for model D1.2, in good agreement with the value for run D1 from Paper II, which is listed in Tab. 3. As can also be seen from Fig. 7, the value of  $(2.98 \pm 0.77) \times 10^{-4}$  for model D1.4 is somewhat reduced. This is consistent, however, with the lower inferred coherence time in this case.

To be more specific, let us compare the prediction based on (6) with the measurement of  $C_\sigma(\Delta x)$ , which can be related via (7). For model D1.1, we infer a spread of  $\Delta a = 0.00161$  au at a distance of  $a_0 = 5$  au, and after a run-time of  $t - t_0 = 200$  orbits. This value may readily be checked by reading it off the right hand axis of Figure 7. By means of specifying  $\tau_c$  and  $\sigma(\Gamma_y)$ , the diffusion equation predicts  $\Delta a = 0.00148$  au, which is only about ten percent smaller than the actual value. A similar comparison for model D1.2 yields  $\Delta a = 0.00154$  au from Fig. 7, opposed to an estimated 0.00140 au from the diffusion approach, i.e., agreement again to within ten percent. Finally, for model D1.4 we predict  $\Delta a = 0.00122$  au via (6), and observe a value of 0.00105 au, which is about 15% smaller than the estimated value. Compared to the results from Paper II, this means a substantially improved accuracy of the predictions. We attribute this to the more stationary behaviour of the new simulations effected by the inclusion of super-box scale dissipative effects (cf. Sect. B2). We conclude that the simplified description of particle spreading in terms of a diffusion equation can be used as a reliable tool in predicting the level of dispersion in the immersed planetesimal population within a dead zone. Moreover, the good agreement between the estimated and measured values lends support to the accuracy of the coherence times fitted via (5).

### 3.6 Eccentricity stirring

To complete our discussion on how the embedded planetesimals are affected by the turbulence, we now briefly consider the excitation of their eccentricity. This has been done in some detail in section 5 of Paper II, including a discussion of the long-term evolution and related saturation mechanisms. In this section, we consider the results of the simulations directly, and leave discussion about their implications for planetesimal accretion and planet formation theory until later in Sect. 6 of this paper.

Figure 8 shows that the rms eccentricity curves for the different models resemble a braided band. Owing to the modest number of embedded particles, the chance fluctuations are quite pronounced again. We register an overall spread of the curves of about a factor of two, which explains the scatter in the fitted amplitudes,  $C_\sigma(e)$ , describing the random-walk curve

$$\frac{\sigma(e)}{H/r} = C_\sigma(e) \sqrt{t}. \quad (8)$$

The values are listed in the last column of Tab. 3, and as a whole agree markedly well with the result from the earlier run D1 from Paper II (see Table 3 in that paper). The striking agreement of the three very different simulations D1.1-4 in terms of their effect on embedded particles again highlights the rather stark disagreement with a scaling proportional to the midplane density fluctuations  $\delta\rho$ . This will be discussed in detail in Section 5, and the implications of the obtained stirring relations for planetesimal evolution will be discussed in Sect. 6. Having established the dependence on the disc

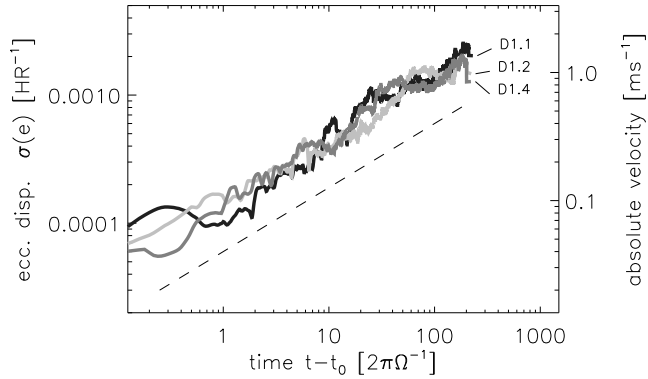


**Figure 8.** Comparison of the rms random-walk eccentricity  $\sigma(e)$ , of sets of 25 particles in runs D1.1–4. The dashed line shows the expected  $\sqrt{t}$  behaviour. The second ordinate indicates the radial velocity dispersion amongst the particles in absolute units. The stirring amplitude is virtually identical in all three runs.

mass, we now move on to the effect of the external net flux permeating our simulation box.

#### 4 DEPENDENCE ON EXTERNAL MAGNETIC FIELD

In the previous discussion, as well as in Papers I and II, we have tacitly assumed a fiducial value of about 10 mG for the net vertical magnetic field permeating the accretion disc (see third column in Tab. 3). This particular value was chosen to produce a turbulent transport coefficient compatible with commonly accepted T Tauri accretion rates. In a global picture, such a field naturally arises from local fluctuations – i.e., it would be hard to imagine that all the various subsections of a disc manage to retain zero vertical flux at the same time. Sorathia et al. (2010) have recently verified this notion by dissecting global zero-net-flux simulations into shearing-box size portions, and found that the turbulent stresses from the emerging dynamo field match the scaling derived from local box simulations with an equivalent imposed vertical net-flux. While their simulations did not include explicit dissipation terms, there is no obvious reason why this correspondence should be lost in global models including dead zones (Dzyurkevich et al. 2010). Note, however, that from unstratified local simulations Fleming et al. (2000) found a critical  $Rm_c \approx 10^4$  necessary to sustain MRI in a zero-net-flux configuration. This threshold was recently confirmed for stratified discs by Oishi & Mac Low (2011). Looking at Fig. 1, we see that this criterion is only met above about  $3.5 H$  in our models, leaving very little space for a self-sustained dynamo mechanism. Because convergence is much harder to obtain without a net flux (see e.g. Davis et al. 2010, and references therein), we consider only runs that include net flux vertical fields in this work.

As an alternative to a dynamo-generated disc field, one might envisage an external stellar field permeating the disc. Given the highly dynamical star-disc interaction during the T Tauri phase, strong magnetic fields are to be expected, and observations find stellar surface fields of roughly 2 – 3 kG (Bouvier et al. 2007). Assuming a dipolar field geometry implies a scaling of  $B = B_\star (R_\star/r)^3$ , and taking  $B_\star = 3$  kG, and  $R_\star = 2 R_\odot$ , we arrive at  $\bar{B}_z \sim 2.4$  mG, and  $\sim 20 \mu\text{G}$  at  $r = 1$  au, and  $r = 5$  au, respectively. Clearly, the contribution of the central star is very moderate at 5 au, but should be considered when looking at models further in. In the following, we will ignore the actual origin of the precise value of

the imposed field, and simply study how a varying level of the field strength influences our results.

#### 4.1 Preliminary considerations

On theoretical grounds there are two effects which determine the expected level of turbulence: (i) the unmistakable scaling of the turbulent stresses with the net flux, and (ii) the extent to which turbulent activity in the MRI-sustaining regions can penetrate into the poorly ionised layer near the midplane. As for the first dependence, it is now safely established that the saturated state of the MRI depends critically on the net field (Hawley et al. 1995; Pessah et al. 2007), and as Yang et al. (2009) have shown from unstratified simulations without dead zones, this should translate directly into the level of turbulent stirring (cf. their fig. 3). In the following, we will set out to explore how this scaling is affected by a dead zone and try to establish the limits of its applicability.

In the case of a net vertical flux (NVF), the most powerful MRI modes are so-called channel flows, i.e. axisymmetric solutions of the perturbed magnetic and velocity fields, only depending on the vertical coordinate  $z$ . It is a remarkable property of these modes that they remain exact solutions of the underlying equations far into the non-linear regime; this property even persists in stratified discs (Latter et al. 2010). Given the large-scale nature of these dominant MRI modes, the question arises whether the flow pattern can efficiently be broken-down into unordered motion. It is commonly accepted that this transition into turbulence happens via parasitic instabilities (Goodman & Xu 1994; Pessah & Goodman 2009; Latter et al. 2009) feeding on the unstable MRI modes. A detailed analysis of how these modes look in the case of a stratified disc can be found in sect. 4 of Latter et al. (2010). The key findings of this analysis are that (i) the parasitic modes have wavelengths of about  $\lambda_{\text{MRI}}/2$ , and (ii) their growth rates are considerably reduced compared to the unstratified case. The latter finding leads to the conclusion that channel flows are expected to be persistent, if not dominant, features in stratified discs. This notion is supported by the ‘streaks’ seen in the density fluctuations (lower-most panels in Figs. 10 and 11), which are remarkably similar to the pinching effect in fig. 3 of Latter et al. (2010). Further evidence for the strong presence of channel modes comes from the horizontally averaged radial and azimuthal velocities  $\bar{u}_r$ , and  $\bar{u}_\phi$  (not shown), which exhibit a remarkable correlation with  $\bar{B}_r$ , and  $\bar{B}_\phi$ , and notably show the opposite parity compared to their magnetic counterparts. This symmetry is highly indicative of the solutions derived in Latter et al. (2010), cf. their fig. 1, and a direct consequence of the underlying set of equations. To conclude this digression, we note that while the presence of MRI channels was already mentioned in Paper II, their appearance is even more pronounced when going to higher field strength.

#### 4.2 Turbulence amplitude as a function of net-flux

In the left panel of Fig. 9, we plot the time- and volume-averaged transport coefficients obtained from runs D1-NVFa/b, covering a range of  $\bar{B}_z = 2.68 - 43$  mG (i.e. field strengths spanning a factor of sixteen). We want to point out that this interval roughly coincides with the practical limits set by the MRI wavelength,

$$\lambda_{\text{MRI}}(z) \equiv \frac{2\pi}{\Omega_0} \sqrt{\frac{15}{16} \frac{|\bar{B}_z|}{\sqrt{\rho(z)}}}, \quad (9)$$

of the fastest-growing linear mode. At the weak-field end, the wavelength is just long enough to be well-resolved, while at the strong-

**Table 3.** Overview of simulation results including runs from papers I & II. For reference, we list the net vertical field  $\langle B_z \rangle$  (col. 3) which serves as an input parameter. All turbulent stress parameters (cols. 4-6) are normalised by the midplane pressure of model D1, i.e.,  $p_0 = 1$ . Relative fluctuations  $\delta\rho/\rho$  are midplane values. The width  $\sigma(\Gamma_y)$  of the torque amplitude is obtained from Fig. 5, correlation times  $\tau_c$  are from the ACFs in Fig. 6, and  $C_\sigma(\Delta x)$  and  $C_\sigma(e)$  are derived from Figs. 7 and 8, respectively. Note that runs NVF a/b apply different  $\tau_{\text{diff}}$  (cf. Eqn. (B3) in Sect. B2), assuming  $k_r = \pi/r$ , and  $2\pi/r$ , respectively.

	orbits	net $\langle B_z \rangle$ [mG]	$\langle \alpha_{\text{Maxw}} \rangle$	$\langle \alpha_{\text{Reyn}} \rangle$	$\langle \alpha_{\text{SS}} \rangle$	$\delta\rho/\rho$	$\sigma(\Gamma_y)$ [cm <sup>2</sup> s <sup>-2</sup> ]	$\tau_c$ [2 $\pi\Omega^{-1}$ ]	$C_\sigma(\Delta x)$ [H]	$C_\sigma(e)$ [H/r]
A1	20-217	10.7			0.0105	–	$0.45 \times 10^8$	0.30	$5.21 \times 10^{-3}$	$2.68 \times 10^{-3}$
D2	20-223	10.7			0.0051	0.166	$0.13 \times 10^8$	0.27	$7.25 \times 10^{-4}$	$2.50 \times 10^{-4}$
B1	20-505	16.1			0.05	0.168	$0.74^a \times 10^8$	0.32	$7.70 \times 10^{-3}$	$2.77 \times 10^{-3}$
D1	20-224	10.7			0.0038	0.103	$0.06 \times 10^8$	0.29	$4.72 \times 10^{-4}$	$1.54 \times 10^{-4}$
D1.1	20-230	10.7	$3.17 \times 10^{-3}$	$0.64 \times 10^{-3}$	0.0038	0.091	$0.054 \times 10^8$	0.30	$4.56 \times 10^{-4}$	$1.67 \times 10^{-4}$
D1.2	20-222	10.7	$3.22 \times 10^{-3}$	$0.59 \times 10^{-3}$	0.0038	0.058	$0.052 \times 10^8$	0.29	$4.36 \times 10^{-4}$	$1.13 \times 10^{-4}$
D1.4	20-221	10.7	$2.75 \times 10^{-3}$	$0.55 \times 10^{-3}$	0.0033	0.038	$0.052 \times 10^8$	0.22	$2.98 \times 10^{-4}$	$1.27 \times 10^{-4}$
D1.4b	20-75	5.37	$0.19 \times 10^{-3}$	$0.86 \times 10^{-3}$	0.0010	0.021	$0.028 \times 10^8$	0.24	$1.72 \times 10^{-4}$	$6.68 \times 10^{-5}$
D1-WF	40-220	2.68	$0.46 \times 10^{-4}$	$0.22 \times 10^{-3}$	0.0003	0.020	$0.009 \times 10^8$	0.25	$0.61 \times 10^{-4}$	$3.02 \times 10^{-5}$
D1-NVF a	35-50 <sup>b</sup>	2.68	$0.47 \times 10^{-4}$	$0.22 \times 10^{-3}$	0.0003	0.029	$0.009 \times 10^8$	0.26	–	–
	60-90	5.37	$0.20 \times 10^{-3}$	$0.79 \times 10^{-3}$	0.0010	0.048	$0.023 \times 10^8$	0.29	–	–
	100-130	10.7	$0.62 \times 10^{-3}$	$2.94 \times 10^{-3}$	0.0036	0.087	$0.050 \times 10^8$	0.33	–	–
D1-NVF b	20-50	10.7	$0.62 \times 10^{-3}$	$3.27 \times 10^{-3}$	0.0039	0.089	$0.054 \times 10^8$	0.34	–	–
	60-90	21.5	$1.65 \times 10^{-3}$	$1.04 \times 10^{-2}$	0.0120	0.130	$0.062 \times 10^8$	0.26	–	–
	100-130	43.0	$4.89 \times 10^{-3}$	$3.43 \times 10^{-2}$	0.0392	0.134	$0.049 \times 10^8$	0.23	–	–

<sup>a</sup>corrected for 2D/3D evaluation (cf. fig. 8 in Paper I), <sup>b</sup>restricted time interval due to transient ringing at beginning of simulation

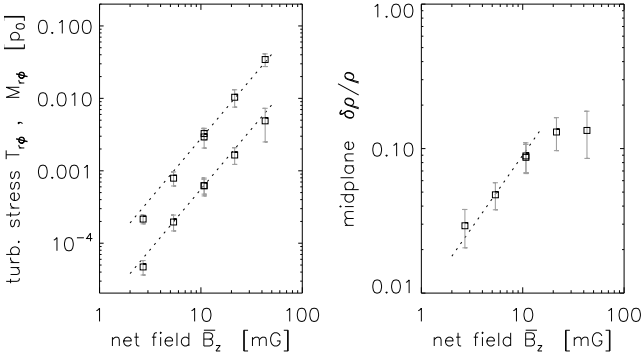


**Figure 9.** *Left:* Scaling of the dimensionless transport coefficients  $T_{r\phi} \equiv \langle \rho v_r \delta v_\phi \rangle$ , and  $M_{r\phi} \equiv \langle -\delta B_r \delta B_\phi \rangle$ . The stresses roughly scale with  $\bar{B}_z$  to the power of 5/3, as indicated by the dotted lines. *Right:* Scaling of the relative density fluctuation  $\delta\rho/\rho$ , measured at the disc midplane. Saturation is reached for  $\sim 20$  mG; below this value, the slope is approximately linear.

field end the wavelength approaches the disc thickness (even at the base of the active layer). These geometric conditions apply to the case of ideal MHD, and hence are in addition to the requirement  $\Lambda > 1$ , describing the resistive quenching of the MRI. Note that because of the z-dependence of the gas density  $\rho(z)$ , the vertical band supporting MRI-unstable wave numbers will successively shift towards the midplane when increasing  $\bar{B}_z$ . In the limit of strong fields, this means that the MRI will be increasingly affected by the  $\Lambda > 1$  criterion. At the same time, the vertical extend of the MRI-active band situated between the magnetically-dominated halo and the resistively-quenched dead zone is expected to shrink, eventually shutting off the MRI altogether.

Within the permissible range described above, we find that the Maxwell stress follows the scaling  $\propto \lambda_{\text{MRI}}^{5/3}$ , which is considerably steeper than the linear dependence proposed by Pessah et al. (2007) – see their fig. 2 – and somewhat steeper than the 3/2 dependence suggested by Sano et al. (2004). We stress that this does not pose

any inconsistency as the earlier results were obtained for the simplified case of unstratified MRI. Pessah et al. (2007), in fact, point out that their results are likely to be modified when accounting for the buoyant loss of magnetic energy in the stratified case (this loss is clearly seen in Figs. 10 and 11 below).

In passing we note that the canonical mass accretion rate observed in T Tauri stars is  $10^{-8} M_\odot \text{ yr}^{-1}$ , and for disc masses similar to the minimum mass model this translates into a viscous stress parameter  $\alpha_{\text{SS}} \sim 0.01$  (Hartmann et al. 1998). This value can indeed be achieved in models below the strong-field limit of the MRI. Setting aside the significant uncertainties in constraining T Tauri accretion rates, this raises the question whether or not a net field of around 20 mG (required to generate the observed typical mass accretion rate) can be sustained by a self-consistent accretion-disc dynamo, or can be dragged in by the accretion flow that is fed by infall from the parent molecular cloud.

While the turbulent stress, at very best, shows a weak break around field strengths of about 10 mG, the derived midplane density fluctuation  $\delta\rho/\rho$  (see right-hand panel of Fig. 9) shows a clear saturation in the strong-field limit. To understand this saturation, we again need to take a look at the vertical structure of the disc.

### 4.3 Disc structure at varying net-flux

Let us recall that in Section 3, the density fluctuations at the disc midplane appeared to be determined by the wave energy available at the dead zone interface defined by the  $\Lambda = 1$  condition. For models D1.1-4, the region where the MRI operated was limited by the column density - i.e. by the disc material being more efficient in shielding exterior sources of ionisation at higher mass loading. Because the Elsasser number at the same time depends on the Alfvén speed, and hence the magnetic field strength, we expect the position of the layer interface to depend on the external net flux.

This dependence is clearly seen in Fig. 10, where we plot the same quantities as in Fig. 2, along with the  $\Lambda = 1$  interface for

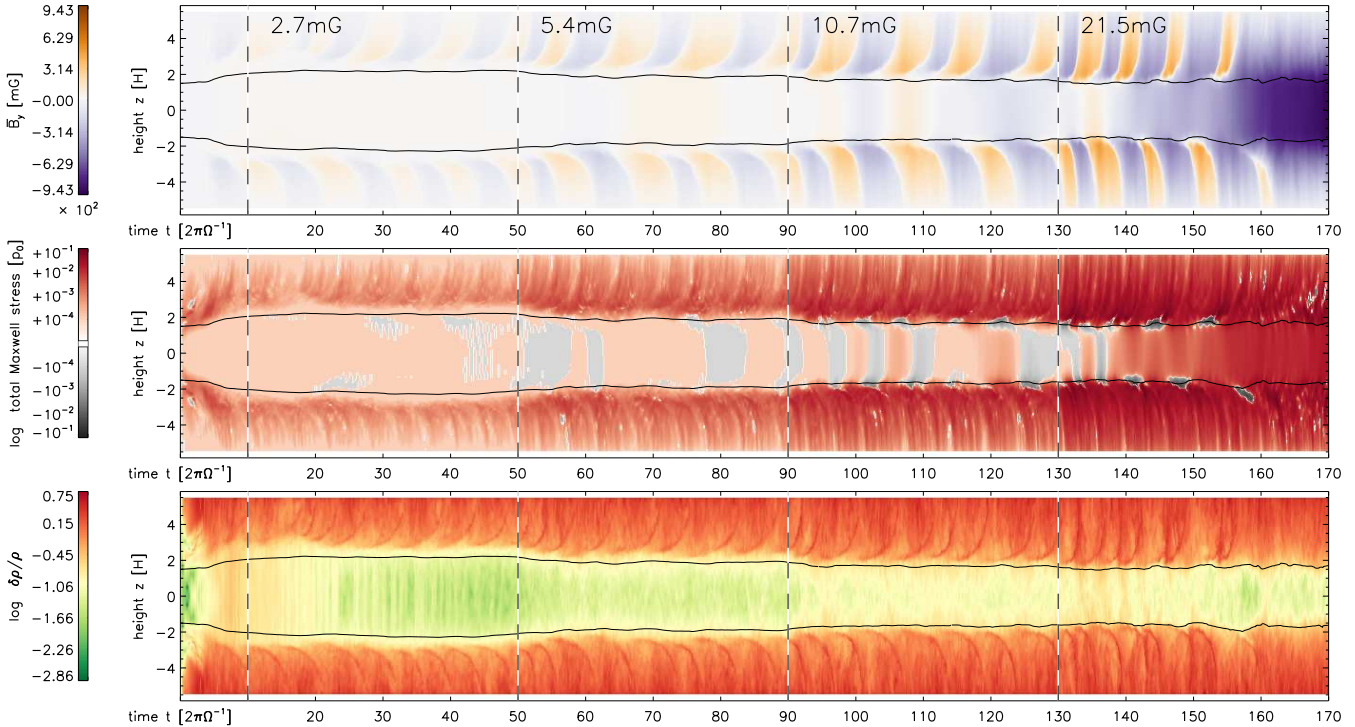


**Figure 10.** Space-time evolution of the mean toroidal field (upper row), total Maxwell stress (middle row), and relative density fluctuation (bottom row) for run D1-NVFa. The solid black line shows the transition between the MRI-active region and the dead zone, approximated by the condition  $\Lambda \equiv v_A^2/(\Omega\eta) = 1$ . Segmentation indicates intervals with different net vertical field strengths of  $\bar{B}_z = 2.68, 5.37, 10.73, 21.47$  mG, respectively. The third interval, from 90 to 130 orbits corresponds to model D1.1, with a net field of 10.73 mG. When obtaining time-averaged quantities, the first 10 orbits of each interval are disregarded.

the run D1-NVFa. We remind the reader that in this simulation we increase the net-flux by a factor of two every forty orbits to examine how the dead zone structure changes (along with the stochastic forces experienced by embedded planetesimals). The half-width of the respective dead zones are  $2.22 \pm 0.03$ ,  $1.89 \pm 0.04$ , and  $1.67 \pm 0.04$  for the first three intervals indicated in Fig. 10. This implies that doubling the net flux, in this regime, decreases the extent of the dead zone by about a third of a scale height – a trend that is equivalent to the one seen in Sect. 3 when reducing the column density by a factor of two. We note that this direct correspondence, however, is only valid for weak fields.

To study stronger net vertical fields, we have to overcome an obstacle which becomes obvious in the last segment of Fig. 10, where we observe a strong build-up of toroidal net flux caused by radial field. Diffusing into the midplane region, this radial flux generates strong azimuthal fields through the differential rotation. According to Kim & Ostriker (2000), the linear growth rate for axisymmetric MRI modes goes asymptotically to zero at low  $\beta_p$  if the field has a significant toroidal component; this likely explains the disappearance of the field reversals and density streaks (associated with channel modes) as  $\bar{B}_\phi$  grows. As discussed in detail in Sect. B2, the winding-up of azimuthal field is artificially enhanced within the shearing box approximation and would be counter-acted by radial diffusion within a global setup. While we thwart this artificial build-up via an extra dissipative term (B4) in the induction equation, the adopted time-scale turned out to be insufficient for net fields exceeding 20 mG. As a remedy, we devised an additional simulation run ‘D1-NVfb’ adopting a more conservative estimate for  $\tau_{\text{diff}}$ , with dissipation faster by a factor of four. For the new run we chose an initial net field of 10.7 mG, which enables us to monitor the effect of the increased field dissipation term by comparing

with the equivalent segment of run D1-NVfb. As can be verified by inspection of the respective lines in Tab. 3, the derived quantities agree to within 10% between the corresponding segments (i.e., orbits 100-130 of NVFa, and orbits 20-50 of NVfb). Moreover, the good agreement *a posteriori* supports our inclusion of the additional magnetic diffusion term.

Space-time plots for run D1-NVfb are shown in Fig. 11, where we see that for fields stronger than about 40 mG, MRI cannot be sustained and the disc returns to a non-turbulent state. Interestingly, in this limit we still observe sporadic bursts of activity (partly restricted to one ‘hemisphere’ of the disc). As above for run D1-NVFa, we infer the half-thickness of the dead zone by means of the  $\Lambda = 1$  criterion, and we yield  $1.66 \pm 0.03$ ,  $1.54 \pm 0.04$ , and  $1.49 \pm 0.10 H$ , for a net-flux field  $\bar{B}_z = 10.7, 21.5$ , and 43 mG, respectively. We conclude that by increasing the field strength we narrow the MRI-active region sandwiched between the dead zone and magnetically-dominated halo, at the same time approaching a limit in the vertical position of the dead zone interface. Accordingly, the magnitudes of fluctuations  $\delta\rho$  at the midplane saturate along with the stochastic torques, as displayed in the right and left panels of Figs. 9 and 12, respectively.

#### 4.4 Gravitational torques as function of net-flux

Unlike the runs with varying disc mass discussed earlier in this paper, we did not evolve the trajectories of embedded particles over time periods of  $\sim 200$  orbits for each value of the magnetic field. Such an approach would be prohibitively expensive computationally. Instead, for most models, we monitor the stochastic torques experienced by embedded particles by accumulating time series, allowing us to infer orbital evolution through analysis of the

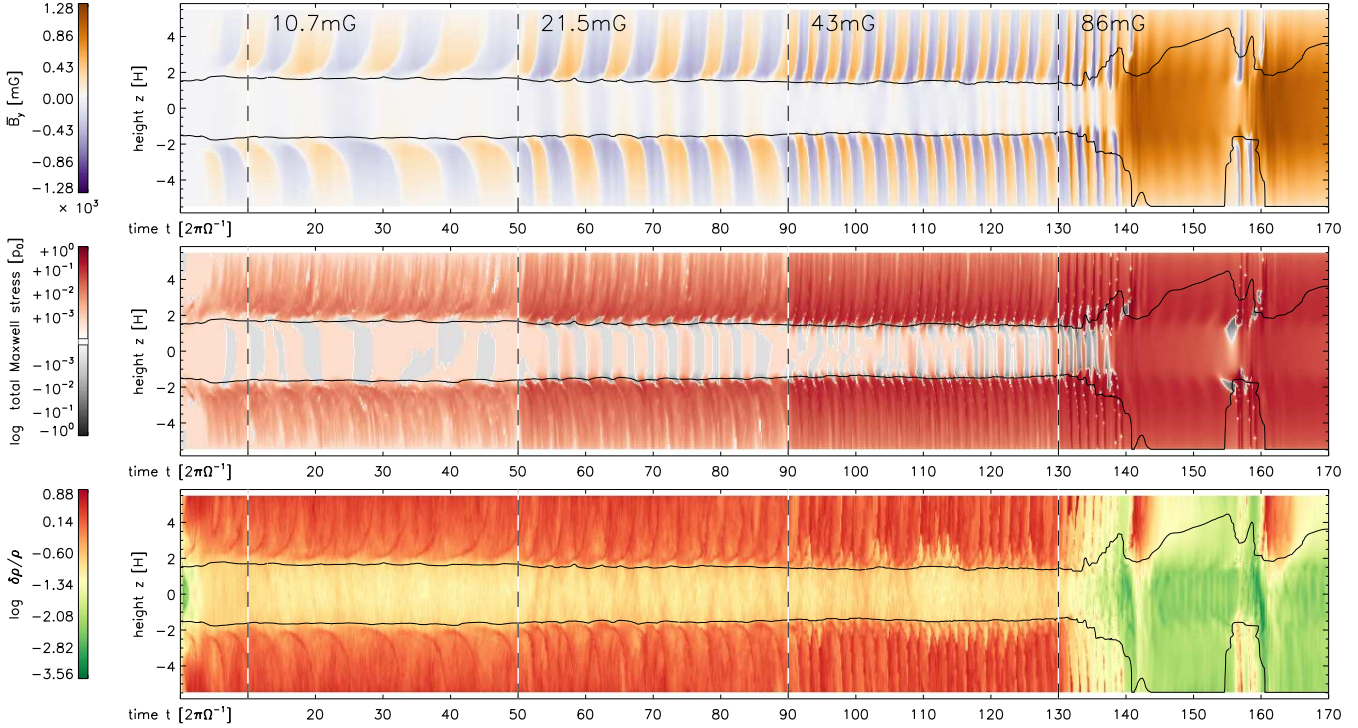


**Figure 11.** Same as Fig. 10, but for run D1-NVfb with a four-times faster super-box-scale dissipation, avoiding the artificial field build-up seen at the end of D1-NVFa. Segments have different net vertical field strengths as indicated. For the strongest field case, we leave the domain in which MRI is possible and the disc returns to a laminar state, interrupted only by short bursts of activity. Note the different colour bar ranges compared to Figure 10.

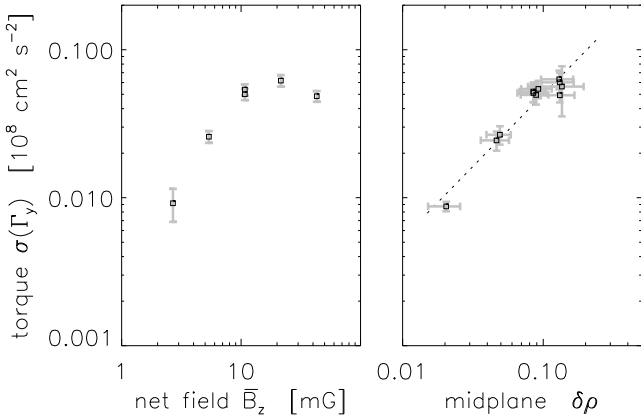


**Figure 12.** *Left:* Scaling of the rms-torque  $\sigma(\Gamma_y)$  with the net vertical field. *Right:* Scaling with the density fluctuation  $\delta\rho$  for runs D1-WF (left-most data point), and D1-NVFa/b; for the latter, each data point represents an interval of  $t = 15$  orbits. The fitted correlation (dashed line) shows a logarithmic slope of 0.97 in good agreement with the expected linear dependence.

widths of the torque distributions  $\sigma(\Gamma_y)$ , and the correlation times  $\tau_c$  (cf. Sect. 3.5 above). For model D1-WF, corresponding to a weak field of 2.7 mG, we evolved the particle trajectories for 200 orbits, and found excellent agreement between the simulation results and expectations based on the simple diffusion model discussed in Sect. 3.5, thus justifying our general approach. The obtained values can be found in the eighth and ninth column of Tab. 3, respectively.

As expected from the density fluctuations plotted in Fig. 9, the gravitational forcing, for magnetic field values below  $\bar{B}_z \approx 10$  mG, depends strongly on the level of the applied field (see left-hand panel of Fig. 12). For field strengths exceeding 10 mG, however,

we find saturation of the fluctuating torques, and this is consistent with the trend found in the density fluctuations in the preceding section. Moderately stronger fields are already MRI-stable and models in this regime are likely to lead to a chaotic time-behaviour of the disc as a whole. Given that we already reached accretion stresses compatible with limits given by observations of T Tauri discs for  $\bar{B}_z = 21.5$  mG, we reckon that the occurrence of even stronger fields seems unlikely. In this sense, the obtained torques of around  $0.05 \times 10^8 \text{ cm}^2 \text{ s}^{-2}$  appear to be a firm upper limit for the given dead zone structure. Higher torques are hence only expected for higher ionising fluxes (cf. model D2 from Paper II) or lower dust abundances (not considered here, but see Turner & Drake 2009), both of which decrease the height of the dead zone.

To conclude our analysis of the results, we note that the range of values in  $\delta\rho$  and  $\sigma(\Gamma_y)$  observed in the three runs D1-WF, and D1-NVFa/b can be used to infer the correlation between the two quantities. Recall that for models D1.1-4, we found a somewhat surprising relation, where a higher value in absolute density fluctuations  $\delta\rho$  would not translate into higher torques. In the limit of high net flux (and accordingly, high density fluctuations), this behaviour is compatible with the scatter seen in the right-hand panel of Fig. 12, where we plot data points sampled from runs D1-WF, and D1-NVFa/b. For weaker turbulence (i.e. for lower values of  $\bar{B}_z$ ), however, we approximately recover the naturally expected linear scaling of  $\sigma(\Gamma_y)$  with the density fluctuations. We conclude that only looking at the rms-value of  $\delta\rho$  in general provides insufficient characterisation of the underlying gravitational stirring – a more sophisticated analysis is required to make quantitative predictions.

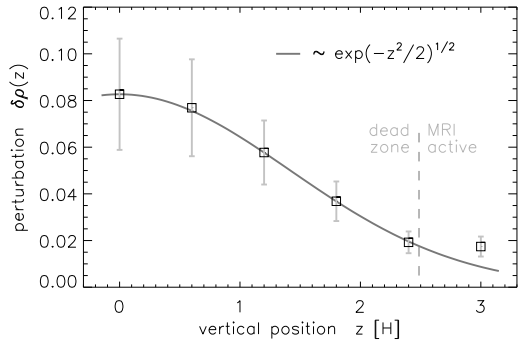


**Figure 13.** Absolute value of the rms density fluctuation  $\delta\rho$  as a function of the vertical position for a model based on D1.4, but with  $B_0 = 5.4$  mG. Within the dead zone, excellent agreement with the theoretically predicted scaling based on the exponential background density profile is seen.

## 5 THE RELATION BETWEEN DENSITY WAVE AMPLITUDE AND GRAVITATIONAL TORQUES

One motivation of this work was to derive intuitive scaling relations that would allow stochastic torque amplitudes to be expressed as simple functions of the disc model parameters. Such functions would provide straightforward prescriptions for gravitational stirring by turbulent discs with application to secular evolution models of planetesimal accretion, et cetera. The original strategy to achieve this aim was to break the problem down into three parts, i.e. (a) predicting the extent of the dead zone and the amplitude of the turbulence as a function of disc mass and external net flux, (b) predicting the resulting amplitude of the induced spiral density waves (characterised by the rms density fluctuation  $\delta\rho$  near the disc midplane), and (c) predicting the associated gravitational torque experienced by the embedded solids. The third step is particularly important as the evaluation of gravitational torques within direct simulations is computationally very expensive when large numbers of particles are being evolved.

In a recent paper, Okuzumi & Hirose (2011) have derived simple predictor functions covering the first two steps outlined above. With respect to the third step, it is natural to assume that the resulting torques scale linearly with the density fluctuation  $\delta\rho$ , but contrary to our own expectations, we find that this assumption is not justified in the presence of a dead zone. Knowledge of  $\delta\rho$  alone is insufficient to construct a simple scaling relation that describes the gravitational stirring of planetesimals. Indeed the results presented in Sect. 3 are in stark conflict with this conjecture. In the following, we will elucidate how the discrepant findings can be reconciled. In our discussion, we are guided by the simple picture of density waves being excited in the active layer and then propagating into the dead zone, where they induce the gravitational stirring experienced by the planetesimals. We will further refine this picture to include the effect of the background differential rotation, as appears necessary to explain the results of our simulations. Finally, we define a set of analytic formulae that provide a means of estimating stochastic torque amplitudes as a function of disc parameters.

### 5.1 Effects due to background shear

We recall from the discussion in Sect. 3.1 that absolute density fluctuations at the disc midplane should obey a scaling  $\delta\rho_{\text{mid}} \propto \sqrt{\rho_{\text{mid}}}$ , which is indeed observed when comparing models D1.1, D1.2, and D1.4, respectively. The agreement in predicting  $\delta\rho$  is independently confirmed when looking at vertical profiles of  $\delta\rho(z)$ . While we only

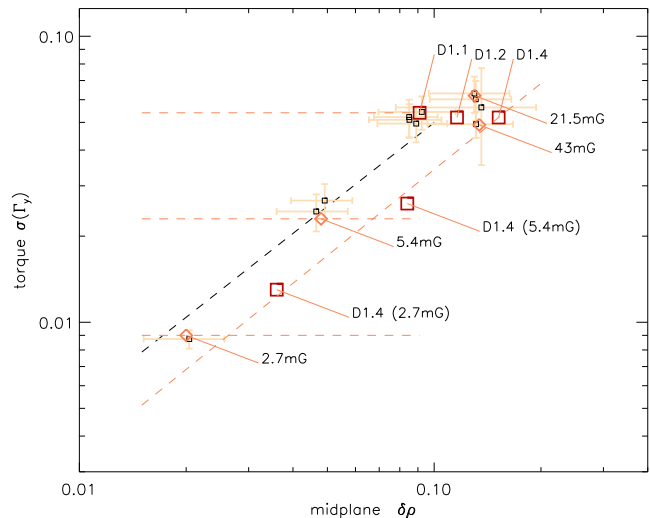


**Figure 14.** Model overview of the  $\delta\rho$  versus torque relation. The shaded data points with error bars are taken from Fig. 12 and complemented by time-averages taken over  $t = 30$  orbits (diamonds). These points represent model D1.1 at varying external flux. Additional points (squares) are as labelled. Dashed lines indicate a linear and constant scaling, respectively.

used two particular positions (i.e. the interface and the midplane) in our previous discussion, we note that the derived relation should equally hold for any position within the disc, i.e.,  $\delta\rho(z) \propto \sqrt{\rho(z)}$ . This is plotted in Fig. 13, where error bars indicate the deviation arising from temporal fluctuations within the adopted time interval  $t = 20 - 85$  orbits. The excellent agreement with the predicted scaling confirms the assumption based on conservation of wave energy, and leads to the conclusion that step (b) in the procedure outline above is justified.

We now contrast the assumption of linear dependence between the absolute density fluctuation  $\delta\rho$  and its associated torque  $\sigma(\Gamma_y)$  – to be used in step (c) – with the results obtained from a comprehensive set of numerical simulations. Figure 14 compiles all available data points in the  $\delta\rho$  versus  $\sigma(\Gamma_y)$  plane, including the ones previously shown in the right-hand panel of Fig. 12 (i.e. for the dependence on the vertical net flux). We have also included additional runs in Fig. 14, performed to provide improved coverage of the  $\sigma(\Gamma_y) - \delta\rho$  plane. These runs were for the heavier disc D1.4 but with external magnetic field values  $\bar{B}_z = 5.4$  and 2.7 mG (labelled in the figure). Clearly the scatter seen in the plot cannot be reconciled with a single linear relation between  $\delta\rho$  and the resulting torque. Let us hence focus on a few particular sub-sets of models first.

Evidently, the torque remains constant<sup>4</sup> when going from model D1.1 to D1.2, and D1.4 as discussed already in Section 3. In contrast, the torques for model D1-NVFa/b (with varying net-flux at constant disc mass), are consistent overall with a linear scaling – although the torques exhibit a somewhat steeper than linear fall-off as a function of  $\delta\rho$  for  $\delta\rho \lesssim 0.1$ . The same trend holds for the additional set of runs based on model D1.4 but with varying net flux (cf. the red squares on the lower right in Fig. 14) – here very little deviation from the linear scaling is seen. The most apparent discrepancy arises between model D1.1 and a four-times heavier

<sup>4</sup> Note that a similar pattern (of a too-low torque at increased disc mass) holds when comparing D1.1 and D1.4 at weaker fields (i.e., 5.4 mG, and 2.7 mG), albeit the effect is seen strongest at 10.7 mG.

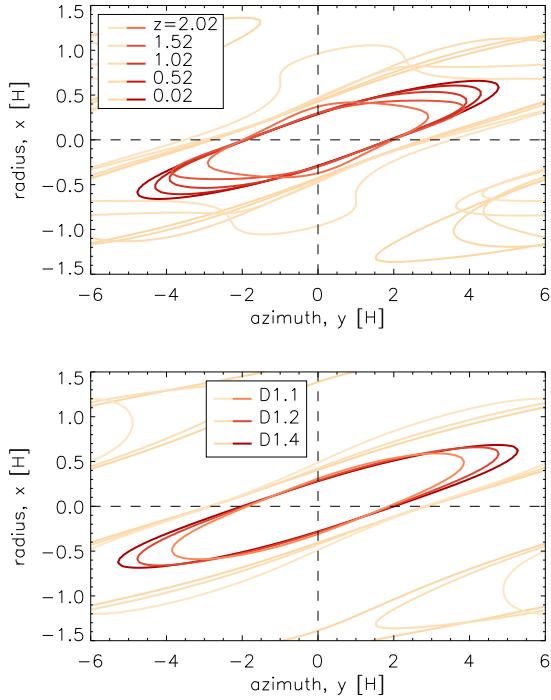


**Figure 15.** *Top:* Contours of the two-point density correlation function for model D1.2 at various vertical positions in the disc. The five dark contours show where the functions fall below  $1/e$  of their peak values; light contours represent the first zero-crossings. *Bottom:* Comparison of the two-point ACF computed within  $z = \pm H/2$  of the disc midplane, for models D1.1-4 (also cf. figs. 3 & 6 in Paper I), showing the same trend as above, but now due to the different width of the respective dead zones.

disc at half the vertical net-flux, labelled ‘D1.4 (5.4 mG)’. While these models agree in the midplane value of  $\delta\rho$  to within 10%, they differ in their effective torques by a factor of two. This clearly demonstrates that there has to exist a significant *qualitative* difference in the density structure between the two models. The obvious difference between the strong-field/low-mass model and the weak-field/high-mass model is the width of the resulting dead zone. As we will see in the following discussion, this observation provides the key to understanding the apparent discrepancy.

### 5.1.1 Two-point density correlation

In the following, we build on the picture of linear sound waves transporting density perturbations into the dead zone region as outlined in Sect. 3.1. We conjecture that the shearing-out of these radially and vertically propagating spiral density waves affects the torque distribution inferred near the disc midplane. This picture gains support from looking at the two-point correlation of the gas density, which we compute in horizontal slabs of vertical extent  $z = \pm H/2$ , and which we average over  $t = 20 - 220$  orbits. The two-point ACF of the density field serves as a qualitative indicator for the degree of coherence in the density structures and was used in Paper I to compare local and global models of fully active MRI. To trace the characteristic evolution of the propagating density waves, we compute two-point ACFs at different vertical positions in the disc, starting from the dead/active zone interface and moving towards the midplane in steps of  $H/2$ . This is exemplified for model D1.2 in the upper panel of Fig. 15, but the observed trend holds for

all the studied models. The plot clearly shows that density features, on average, are more sheared-out towards the midplane.

We further conjecture that the stretching arises because the density waves become increasingly sheared out by the background differential rotation as they propagate from the vertical position where they are created down toward the midplane. To estimate the amount of stretching, we assume a vertical propagation speed of  $c_s = H\Omega$ , resulting in a propagation time  $\Delta t = 2H/c_s = 2\Omega^{-1}$  for a dead zone half-width of two scale heights. Assuming Keplerian shear with  $q = 3/2$ , and evaluating at a position  $x \simeq 0.5H$  away from the coordinate origin, this amounts to an azimuthal displacement of  $\Delta y = q\Omega x \Delta t = 3/4 H\Omega \times 2\Omega^{-1} = 1.5H$ , which is in decent agreement with the level of stretching seen in Fig. 15. As a further step, we checked that the characteristic pitch angle for density waves observed at the dead zone interface is the same for all the models.

With this knowledge at hand, we can now attempt to reconcile the results from Sect. 3. Given the significant widening of the dead zone when increasing the disc mass, we expect more sheared-out ACFs for model D1.4 than for model D1.2, and D1.1, respectively. This is because the travel time for waves to reach the planetesimals situated near the disc midplane directly depends on the width of the dead zone. The suggested trend is clearly seen in the lower panel of Fig. 15, where we plot the midplane ACFs for the three models.

The shapes of the ACFs are characteristic of trailing spiral waves, and the degree of correlation in the azimuthal direction shows a clear trend with disc mass. This, in turn, supports the notion that the stronger fluctuations  $\delta\rho$  in the heavier disc models are compensated by the more elongated aspect ratio in the density structures. It is well known that the winding-up of the spiral structures due to differential rotation leads to a linear increase in the radial wave-number  $k_r \propto (3\Omega/2)t k_y$  in time. This process goes along with a phase-folding of the azimuthal structures. The enhanced azimuthal symmetry of increasingly sheared out density waves, as viewed by embedded planetesimals, leads to a reduction in the average amplitude of the stochastic torque due to partial cancellation of the induced azimuthal gravitational acceleration.

### 5.1.2 Modified scaling relation

So far, our reasoning has been largely qualitative. In this section we aim to provide more quantitative evidence of how the simple linear relation between density fluctuations and gravitational torques might have to be modified. Having identified the distance away from the dead zone interface as the relevant parameter determining the pitch angle of the density field (and hence the effective gravitational force), it appears natural to use the dead zone half-width  $h_{\text{DZ}}$  as a parameter to empirically correct our prediction for the resulting torques. This is done in Fig. 16, where we boost the measured torques by a factor  $(h_{\text{DZ}}/2H)^p$ , with  $p$  to be determined. The rescaling is done to restore, as accurately as possible, a linear dependence  $\sigma(\Gamma_y) \propto \delta\rho$ . The particular choice of the fiducial width  $2H$  implies that we pivot around model D1.2, which has this dead zone width and hence remains unaffected. We point out that the rescaled torque amplitude does not have any physical implication but merely serves as a benchmark. In practice, one can use the inverse scaling factor to correct torque estimates based on predicted values of  $\delta\rho$  for the attenuation caused by the stretching. By varying  $p$  and inferring deviations from a power-law, we find a best-fit index of  $p \simeq 5/4$ , which does a reasonable job in collapsing the scatter plot to a single line in log-log space. As indicated by stars in Fig. 16, we excluded the data points with field strengths higher than the nominal

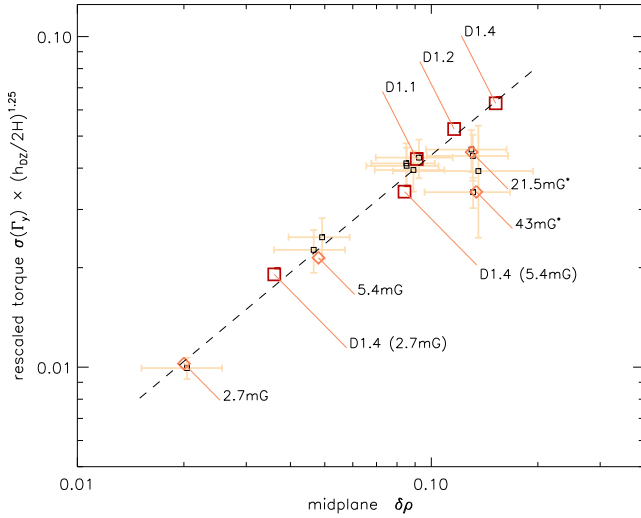


**Figure 16.** Same as Figure 14, but with the torques rescaled by  $(h_{DZ}/2H)^p$  to compensate for the attenuation of the measured torques by the stretching-out of the density field. Excluding the strong-field models (see text), we obtain a best-fit correction parameter of  $p \approx 5/4$ .

value of 10.7 mG. This has been done because in this limit the dead zone width does not change any more, and the stirring amplitude saturates accordingly. We note, moreover, that the resulting slope is somewhat smaller than the expected linear relation. Given the simplicity of the approach, however, we regard this a satisfactory result. As can be seen in Fig. 16, the rescaling mostly affects models with different column densities, and the models D1.1, D1.2, and D1.4 now show the expected linear scaling with  $\delta\rho$ . This also affects the heavy disc models with weaker fields (D1.4 [2.7 mG], and D1.4 [5.4 mG]), which have a wider dead zone. We remark that the rescaling does not destroy the good fit already seen in these models, but at the expense of a power-law index deviating from one. Moreover the slight deviation from the linear relation within the data points belonging to different time intervals in models D1-NVFa/b (diamond-shaped points & D1.1) is now much smaller. Overall we regard the procedure as reasonably successful in correcting for the attenuation of the torque amplitudes suffered because the density waves shear out as they propagate towards the disc midplane. We hence suggest to compensate torque estimates based on  $\delta\rho_{\text{mid}}$  by an extra factor  $(h_{DZ}/2H)^{-1.25}$  with respect to a fiducial model with  $h_{DZ} = 2H$ . Because heavier discs have wider dead zones and hence weaker effective torques (compared to the original scaling based on  $\delta\rho_{\text{mid}}$  alone), in practice, this leads to more favourable conditions for planetesimal accretion in heavier discs, where gas-drag damping of the induced velocity dispersion is enhanced.

## 5.2 A simple stochastic torque prescription

Having derived the additional correction factor for the stochastic torque amplitude as a function of  $h_{DZ}$ , we are now in the position to provide a simple analytic fitting formula that encapsulates all the data points of the studied set of models. We here focus on providing rms torque amplitudes  $\Gamma_y$  and correlation times  $\tau_c$ . Owing to saturation effects, we limit the scope of applicability to magnetic field strengths of  $\bar{B}_z \lesssim 10.7$  mG. We also point out that the derived scalings are only strictly valid for the chosen ionisation model, representative of a protosolar nebula at a distance of  $a = 5$  au, and for a range of column densities around a few times the MMSN.

As we have seen in sections 3 and 4, the width of the dead zone changed by about a third of a scale-height when either doubling the disc mass, or halving the magnetic net-flux, respectively. More precisely, we obtain a half-width

$$h_{DZ} = 1.66 H - \Delta h_B \frac{\ln(\bar{B}_z/10.7 \text{ mG})}{\ln 2} + \Delta h_\Sigma \frac{\ln(\Sigma/135 \text{ g cm}^{-2})}{\ln 2} \quad (10)$$

relative to model D1, and with coefficients  $\Delta h_\Sigma = 0.33 H$ , and

$$\Delta h_B = 0.28 H - 0.04 H \frac{\ln(\Sigma/135 \text{ g cm}^{-2})}{\ln 2}, \quad (11)$$

i.e., accounting for a slightly weaker dependence of  $h_{DZ}$  on the net magnetic field when going to heavier disc models.

The scaling of the rms midplane density fluctuation  $\delta\rho$  with disc mass was derived in Sect. 3.1. Based on the empirical finding of  $\delta\rho_{\text{mid}}/\rho_{\text{mid}} \propto \rho_{\text{mid}}^{-0.63}$ , we here use a power-law index of 0.37, i.e., deviating slightly from the analytically predicted square-root dependence. For the scaling with the vertical net flux, the assumption of a simple linear dependence between  $\delta\rho$  and  $\bar{B}_z$  produced equally good results for the models based on D1.1, and D1.4, respectively. Overall we thus arrive at a predictor function for the rms stochastic torque amplitude of

$$\Gamma_y = \Gamma_{y,D1} \left( \frac{\Sigma}{135 \text{ g cm}^{-2}} \right)^{0.37} \left( \frac{\bar{B}_z}{10.7 \text{ mG}} \right) \left( \frac{h_{DZ}}{1.66 H} \right)^{-1.25}, \quad (12)$$

relative to the fiducial model D1 with  $\Gamma_{y,D1} = 0.054 \times 10^8 \text{ cm}^2 \text{ s}^{-2}$ , and with  $h_{DZ}$  as given by (10), and (11). This formula – together with a canonical value of  $\tau_c \approx 0.3$  orbits – completes our simple prescription for including stochastic torques in generic planetesimal evolution models.

## 6 LONG-TERM EVOLUTION

In Sects. 3.6 and 4.4 we discussed the rate at which the velocity dispersion of planetesimals is excited by gravitational interaction with turbulent density fluctuations in the disc midplane. The driving of the velocity dispersion is counteracted by the combined effects of gas drag and collisional damping (Ida et al. 2008), leading to a well defined equilibrium value for the rms random velocity. We now calculate the approximate magnitude of this equilibrium velocity dispersion and compare it with estimates for the catastrophic disruption thresholds of planetesimals composed of strong or weak materials.

### 6.1 Planetesimal equilibrium velocity dispersions

Following closely the analysis presented in sect. 5.1 of Paper II, we estimate the equilibrium velocity dispersion,  $v_{\text{disp}}$ , for planetesimals of different sizes, and compare it with the catastrophic disruption thresholds for strong and weak aggregates to determine under which conditions collisions between (equal-sized) planetesimals will lead to growth rather than destruction.

Balancing the rate of eccentricity excitation obtained in simulations with the gas drag damping rate, we obtain the following expression for the resulting velocity dispersion (see Paper II for details)

$$v_{\text{disp}} = \left[ \frac{4C_\sigma^2(e)h^2R_p\rho_p v_k^2}{10^9 C_D \rho} \right]^{1/3} \text{ cm s}^{-1}. \quad (13)$$

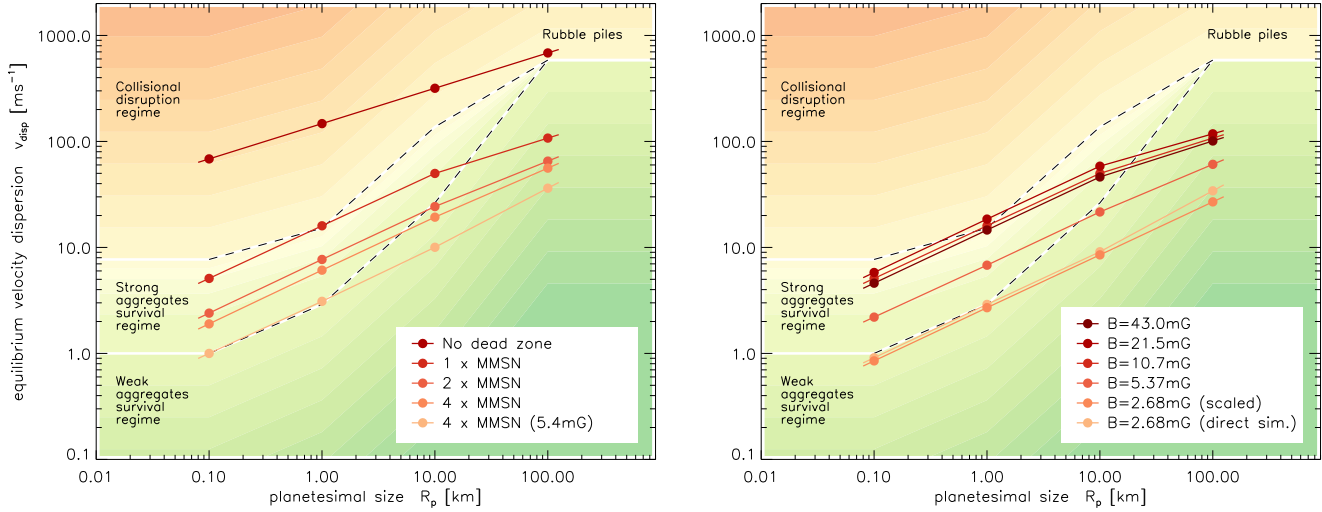


**Figure 17.** *Left:* Variation of the equilibrium velocity dispersion as a function of planetesimal size and the disc mass. Increasing the disc mass increases the midplane density and planetesimal collision probability, thereby increasing gas drag and collisional damping. *Right:* Variation of equilibrium velocity dispersion as function of planetesimal size and magnetic field strength.

Similarly, balancing the rate of eccentricity growth with the mutual collisional damping rate for planetesimals (assuming all solids in the disc have grown into planetesimals of a given size,  $R_p$ , with a mean density  $\rho_p = 2 \text{ g cm}^{-3}$ , and the coefficient of restitution  $\approx 0$ ) gives the expression

$$v_{\text{disp}} = \sqrt{\frac{4R_p \rho_p C_\sigma^2(e) h^2 v_k^2}{10^9 \Sigma_p \Omega_k}} \text{ cm s}^{-1}. \quad (14)$$

The catastrophic disruption thresholds for strong (basalt) and weak aggregates are given by Stewart & Leinhardt (2009), and are discussed in detail in Paper II in the context of planetesimal stirring in turbulent discs. We plot the catastrophic collision velocities in Fig. 17 as a function of planetesimal radius (solid black lines). We assume that the largest 100 km sized bodies are rubble-piles rather than monolithic bodies, and so adopt the appropriate disruption velocity in this limit. In this figure we also plot the equilibrium velocity dispersions for planetesimals of different size from the different simulations. The plotted values correspond to the smaller of those calculated using eqns. (13) and (14). The left panel shows results for different disc masses with a fixed external magnetic field strength of 10.7 mG. The right panel compares results for different magnetic field strengths in a disc with fixed mass (approximately equal to the MMSN model).

The left panel of Fig. 17 shows that planetesimals with radii between 0.1 and 1 km have equilibrium velocity dispersions that lie between the catastrophic disruption thresholds for weak and strong materials when embedded in discs with masses between 1 and 4 times the MMSN. Collision outcomes for these bodies will depend sensitively on the material properties. 10 km bodies in discs with 2 or 4 times the MMSN mass will have velocity dispersions that are marginally lower than the catastrophic disruption thresholds for even weak materials. 100 km-sized rubble piles are clearly safe from disruption in all models. The decreasing equilibrium velocity with increasing disc mass arises because the gas drag scales with the midplane density, the mutual collision rate depends on the number density of planetesimals, and the strength of the stochastic stirring was found to be essentially independent of the disc mass for these models.

Examining the right panel of Fig. 17, we see that reducing the value of the magnetic field leads to a reduction in the stirring of planetesimals. Decreasing the field strength increases the size of the dead zone and reduces the level of turbulence in the active layers. We remind the reader that for most simulations conducted with varying magnetic field strength, the orbital trajectories of particles were not evolved under the influence of disc forces, but instead we monitored the time varying torque due to the turbulent fluctuations acting on the particle swarm. Estimates for the values of  $C_\sigma(e)$  used in eqns. (13) and (14) to calculate the equilibrium velocity dispersions were obtained by assuming a linear scaling between the rms fluctuating torque and  $C_\sigma(e)$ , using the run with  $\bar{B}_z = 10 \text{ mG}$  to provide the normalisation. The validity of this approach is confirmed by the run with  $\bar{B}_z = 2.68 \text{ mG}$  for which particle trajectories were evolved under the influence of disc forces, and for which both the predicted and simulated values of  $C_\sigma(e)$  were found to be in very good agreement, as shown in the right panel of Figure 17. For this run, which contains the weakest field considered, the equilibrium values of  $v_{\text{disp}}$  fall beneath the catastrophic values appropriate for weak aggregates for all planetesimal sizes, suggesting that all bodies will be safe from collisional destruction in such a disc. For stronger fields, however, the values typically lie between the thresholds for strong and weak materials. 100 km-size rubble-piles are again safe from collisional break-up in all models. We note that the predicted mass accretion rate for the disc model with  $\bar{B}_z = 2.68 \text{ mG}$  is rather low, being  $\dot{M} \approx 5 \times 10^{-9} M_\odot \text{ yr}^{-1}$ . This is a factor of two lower than the canonical value of  $10^{-8} M_\odot \text{ yr}^{-1}$  observed for T Tauri stars (Sicilia-Aguilar et al. 2004). The scaling we obtain with field strength and disc mass, however, suggest that a slightly stronger field can generate a larger accretion rate in the active zone, and in a more massive disc than the MMSN the velocity dispersion will remain lower than the catastrophic values for weak materials. This expectation is supported by the simulation D1.4b described in Tab. 3, which used the heaviest disc model D1.4 and an external magnetic field  $\bar{B}_z = 5.4 \text{ mG}$ . Turbulent stresses induce a mass accretion rate  $\sim 2.7 \times 10^{-8} M_\odot \text{ yr}^{-1}$ , and the values of  $v_{\text{disp}}$  are illustrated by the lowest set of points in the left panel of Fig. 17. It is clear that disc models can be constructed that satisfy requirements

on disc accretion rates and allow even the weakest planetesimals to avoid collisional disruption. It is advisable not to over-interpret the results of our study, however, due to the simplifying assumptions that have gone into our calculations. Suffice it to say that we have been able to produce disc models with reasonable accretion rates within which the dead zone provides a safe-haven against catastrophic disruption of planetesimals of all sizes even when they are composed of essentially strength-less materials.

## 6.2 Implications for planet formation

We now summarise the key results from our studies of planetesimals embedded in turbulent discs, focusing on their relevance for planet formation theory. We do this by first providing a brief review of our findings from Papers I and II and then discuss how these are affected in view of the new results obtained in this paper.

In Paper I, we considered the dynamical evolution of small particles (pebbles and boulders) whose interaction with the gas was dominated by gas drag, in addition to larger bodies (planetesimals) whose interaction is dominated by gravitational interaction with turbulent density fluctuations. Particles tightly coupled via gas drag have sizes  $\lesssim 1$  m at 5 au, and were shown to rapidly achieve a velocity dispersion equal to the gas turbulent velocity. At the midplane in a dead zone this velocity is typically  $10\text{--}30$  m s<sup>-1</sup>, possibly slowing protoplanet growth in models that rely on accretion of small particles by planetesimals and embryos (e.g. Rafikov 2004; Johansen & Lacerda 2010; Ormel & Klahr 2010).

We now focus on the evolution of larger bodies whose dynamical evolution is determined by gravitational interaction with turbulent density features. Papers I and II demonstrate that a model of planetesimal formation based on gradual binary sticking of smaller particles cannot operate in a fully turbulent disc due to rapid growth of the velocity dispersion above catastrophic disruption thresholds for bodies of size  $\lesssim 10$  km. Models that invoke rapid formation of large (i.e.,  $\sim 100$  km) planetesimals may operate (e.g. Johansen et al. 2007; Cuzzi et al. 2008), but runaway growth to form larger bodies is not possible because the velocity dispersion quickly rises to the surface-escape velocity of these objects. Forming planets within the disc lifetime appears to be difficult in a fully turbulent disc without a dead zone, unless a model involving gravitational instability is invoked (Boss 1998).

Results from Paper II (and model D1.1 in this work) show that stochastic forcing of planetesimals is  $\sim 20$  times weaker for a minimum-mass disc with a nominal dead zone than in a disc without a dead zone. Equilibrium velocity dispersions for 100 m - 10 km bodies lie between disruption thresholds for weak and strong materials (Stewart & Leinhardt 2009), being between a few metres and a few tens of metres per second (cf. sect. 5.3 in Paper II for details). In principle, planetesimals that form via gradual accumulation can survive mutual collisions in the nominal model if composed of moderate-strength materials. To form in the first place, however, they need to overcome barriers to growth occurring at mm and metre sizes (Brauer et al. 2008; Zsom et al. 2010). 10 km-sized bodies forming gradually will not experience runaway growth to form larger oligarchs as their velocity dispersion reaches  $\sim 10$  m s<sup>-1</sup> within  $\sim 10^5$  yr. Because the dispersion remains below the destruction threshold, further growth can proceed; eventually delayed runaway growth may occur for resulting bodies with  $\sim 100$  km radii (also see Ormel et al. 2010).

Rapid formation of large planetesimals with sizes  $\geq 100$  km through turbulent concentration of chondrules (Cuzzi et al. 2008) or the streaming instability (Johansen et al. 2007) in the nominal dead

zone results in runaway growth because of slow turbulent stirring of the velocity dispersion. Self-stirring by planetesimals determines the dispersion in this case rather than turbulence. We note that all dead zone models predict that 100 km rubble-piles are safe against turbulence-induced collisional destruction.

Increasing the disc mass by a factor of two or four does not dramatically change the above picture, as demonstrated by models D1.2 and D1.4 in Sect. 3. These models result in smaller equilibrium dispersion velocities for larger disc masses because of the constant stirring strength and increased eccentricity damping. Increasing the external magnetic field strength above 10.7 mG increases stochastic forcing and  $v_{\text{disp}}$ , but saturation is attained when the external field approaches values too strong for the MRI to operate in the active zone. Reducing the field strength weakens stochastic forcing by increasing the dead zone width and reducing activity levels in the turbulent layers. A model with  $\bar{B}_z = 2.7$  mG results in  $v_{\text{disp}}$  values below the catastrophic disruption threshold for the weakest aggregates. This important result demonstrates that weak 100 m - 100 km planetesimals can survive collisional destruction in a reasonable dead zone model, albeit one whose mass accretion rate is a factor of two below the canonical mass accretion rate in T Tauri stars (but still within the observed range of values). Model D1.4b demonstrates, however, that a heavier disc with a slightly stronger field can generate a larger mass accretion rate and similar velocity dispersion (see Tab. 3 and Fig. 17). Weaker stochastic forcing leads to slower growth of the velocity dispersion toward the escape velocity of 10 km-sized bodies. The time for the velocity dispersion to reach  $10$  m s<sup>-1</sup> in the weak magnetic field model is  $\sim 3$  Myr, so runaway growth of 10 km-sized bodies can occur in this disc.

## 7 CONCLUSIONS

This is the third paper in a series that examines the dynamics of planetesimals embedded in turbulent protoplanetary discs. In the present work we have used local disc models situated at 5 au that include a simple equilibrium gas-grain chemistry to examine how changing the disc column density and the external magnetic field strength modifies the size of the dead zone, and the level of gravitational stirring of particles located at the disc midplane. We consider column densities that lie approximately between one and four times the minimum mass solar nebula values, and external magnetic field strengths between 2.68 - 43 mG. Our main conclusions can be summarised as follows:

(i) Increasing the disc mass by a factor of two or four above the nominal value for the minimum-mass model leads to the unexpected result that the strength of particle stirring is independent of disc mass. Scaling relations based on a simple picture of linear waves being excited in the active layer and propagating into the dead zone predict that absolute density fluctuations at the midplane will scale with the square-root of the column density. This scaling is observed in the simulations, but gravitational stirring is found to be insensitive to the larger absolute density fluctuations.

(ii) Analysis of two-point correlation functions for the midplane density fields between discs with different dead zone heights show that typical density structures in discs with larger dead zones are more elongated in the azimuthal direction. Density waves propagating from the active layer into the dead zone are more sheared out when they reach the midplane in larger dead zones, resulting in reduced stochastic gravitational forces.

(iii) We suggest this phenomenon explains the insensitivity of planetesimal stirring to increasing disc mass, as is demonstrated by

a scaling-law for the stochastic torques that depends on the dead zone vertical extent, and which accounts reasonably for our simulation results.

(iv) Decrementing the external magnetic field strength increases the size of the dead zone and decreases the level of activity in the turbulent layers. This, in turn, leads to reduced absolute density fluctuations in the disc midplane and corresponding reductions in the level of gravitational stirring experienced by embedded planetesimals.

(v) Moderate increments in the external magnetic field strength reduce the size of the dead zone, and increase the level of activity in the turbulent layers. This, at first, results in an increased stirring of planetesimals, but quenching occurs when the position of the dead zone interface reaches saturation. This is because the amount to which the active layers can constrict the dead zone is limited (via the  $\Lambda = 1$  criterion) by the steep rise in  $\eta(z)$ . For our model, torque fluctuations saturate for  $\bar{B}_z \geq 20$  mG, while turbulent stresses grow up to net fields of  $\approx 40$  mG, where the MRI eventually shuts off.

(vi) A disc hosting a modest external field (of  $\bar{B}_z = 2.7\text{--}5.4$  mG) leads to equilibrium velocity dispersions for 100 m to 10 km planetesimals below the catastrophic disruption threshold for even the weakest aggregates. This demonstrates that reasonable disc models can be constructed in which the dead zone provides a safe-haven for weak planetesimals against collisional destruction.

There remain a number of caveats that we have not yet addressed, and which may modify the detailed conclusions drawn in this paper. These include adoption of a simple equation of state for the disc, and a mono-disperse size distribution for planetesimals when estimating collisional damping rates. The most important omissions are the Hall effect and ambipolar diffusion from the induction equation, which may affect the size of the dead zone and the level of turbulent activity in the active zones (Wardle & Salmeron 2011). Nonetheless, we expect that the main result of our study remains robust, namely that dead zones lead to much reduced stochastic forcing of planetesimal random velocities, and provide potentially benign locations for planetary formation.

## ACKNOWLEDGEMENTS

We thank the anonymous referee for her/his detailed report. This work used the *NIRVANA-III* code developed by Udo Ziegler at the Leibniz Institute for Astrophysics (AIP). All computations were performed on the QMUL HPC facility, purchased under the SRIF initiative. N.J.T. was supported by the Jet Propulsion Laboratory, California Institute of Technology, the NASA Origins and Outer Planets programs, and the Alexander von Humboldt Foundation.

## REFERENCES

- Armitage P. J., 1998, *ApJ*, 501, L189+
- Bai X.-N., 2011, *ArXiv e-prints*
- Bai X.-N., Stone J. M., 2011, *ApJ*, 736, 144
- Balbus S. A., Hawley J. F., 1991, *ApJ*, 376, 214
- Blaes O. M., Balbus S. A., 1994, *ApJ*, 421, 163
- Boss A. P., 1998, *ApJ*, 503, 923
- Bouvier J., Alencar S. H. P., Harries T. J., Johns-Krull C. M., Romanova M. M., 2007, *Protostars and Planets V*, pp 479–494
- Brauer F., Dullemond C. P., Henning T., 2008, *A&A*, 480, 859
- Cuzzi J. N., Hogan R. C., Shariff K., 2008, *ApJ*, 687, 1432
- Davis S. W., Stone J. M., Pessah M. E., 2010, *ApJ*, 713, 52
- Dzyurkevich N., Flock M., Turner N. J., Klahr H., Henning T., 2010, *A&A*, 515, A70+
- Fleming T., Stone J. M., 2003, *ApJ*, 585, 908
- Fleming T. P., Stone J. M., Hawley J. F., 2000, *ApJ*, 530, 464
- Gammie C. F., 1996, *ApJ*, 457, 355
- Garmire G., Feigelson E. D., Broos P., Hillenbrand L. A., Pravdo S. H., Townsley L., Tsuboi Y., 2000, *AJ*, 120, 1426
- Goldreich P., Ward W. R., 1973, *ApJ*, 183, 1051
- Goodman J., Xu G., 1994, *ApJ*, 432, 213
- Gradie J., Tedesco E., 1982, *Science*, 216, 1405
- Gressel O., 2010, *MNRAS*, 405, 41
- Gressel O., Nelson R. P., Turner N. J., 2011, *MNRAS*, 415, 3291
- Gressel O., Ziegler U., 2007, *CoPhC*, 176, 652
- Hanasz M., Otmianowska-Mazur K., Kowal G., Lesch H., 2009, *A&A*, 498, 335
- Hartmann L., Calvet N., Gullbring E., D'Alessio P., 1998, *ApJ*, 495, 385
- Hawley J. F., Gammie C. F., Balbus S. A., 1995, *ApJ*, 440, 742
- Hawley J. F., Stone J. M., 1998, *ApJ*, 501, 758
- Hayashi C., 1981, *Progress of Th. Phys. Suppl.*, 70, 35
- Heinemann T., Papaloizou J. C. B., 2009a, *MNRAS*, 397, 52
- Heinemann T., Papaloizou J. C. B., 2009b, *MNRAS*, 397, 64
- Heinemann T., Papaloizou J. C. B., 2011, *ArXiv e-prints*
- Hirose S., Turner N. J., 2011, *ApJ*, 732, L30+
- Ida S., Guillot T., Morbidelli A., 2008, *ApJ*, 686, 1292
- Ida S., Makino J., 1993, *Icarus*, 106, 210
- Igea J., Glassgold A. E., 1999, *ApJ*, 518, 848
- Ilgner M., Nelson R. P., 2006a, *A&A*, 445, 205
- Ilgner M., Nelson R. P., 2006b, *A&A*, 445, 223
- Ilgner M., Nelson R. P., 2008, *A&A*, 483, 815
- Inutsuka S.-i., Sano T., 2005, *ApJ*, 628, L155
- Jin L., 1996, *ApJ*, 457, 798
- Johansen A., Klahr H., Henning T., 2011, *A&A*, 529, A62+
- Johansen A., Lacerda P., 2010, *MNRAS*, 404, 475
- Johansen A., Oishi J. S., Low M., Klahr H., Henning T., Youdin A., 2007, *Nature*, 448, 1022
- Johansen A., Youdin A., Klahr H., 2009, *ApJ*, 697, 1269
- Kenyon S. J., Bromley B. C., 2009, *ApJ*, 690, L140
- Kim W.-T., Ostriker E. C., 2000, *ApJ*, 540, 372
- Kokubo E., Ida S., 1998, *Icarus*, 131, 171
- Latter H. N., Fromang S., Gressel O., 2010, *MNRAS*, 406, 848
- Latter H. N., Lesaffre P., Balbus S. A., 2009, *MNRAS*, 394, 715
- Lissauer J. J., et al., 2011, *Natur*, 470, 53
- Marois C., Zuckerman B., Konopacky Q. M., Macintosh B., Barman T., 2010, *Nature*, 468, 1080
- Mayor M., Queloz D., 1995, *Nature*, 378, 355
- Nelson R. P., 2005, *A&A*, 443, 1067
- Nelson R. P., Gressel O., 2010, *MNRAS*, 409, 639
- Nelson R. P., Papaloizou J. C. B., 2004, *MNRAS*, 350, 849
- Oishi J. S., Mac Low M., Menou K., 2007, *ApJ*, 670, 805
- Oishi J. S., Mac Low M.-M., 2011, *ArXiv e-prints*
- Okuzumi S., Hirose S., 2011, *ApJ*, 742, 65
- Ormel C. W., Dullemond C. P., Spaans M., 2010, *Icarus*, 210, 507
- Ormel C. W., Klahr H. H., 2010, *A&A*, 520, A43
- Pessah M. E., 2010, *ApJ*, 716, 1012
- Pessah M. E., Chan C., Psaltis D., 2007, *ApJ*, 668, L51
- Pessah M. E., Goodman J., 2009, *ApJ*, 698, L72
- Pneuman G. W., Mitchell T. P., 1965, *Icarus*, 4, 494
- Rafikov R. R., 2004, *AJ*, 128, 1348
- Rayleigh L., 1917, *Royal Society of London Proceedings Series A*, 93, 148
- Safronov V. S., 1972, *Israel Program for Scientific Translation*

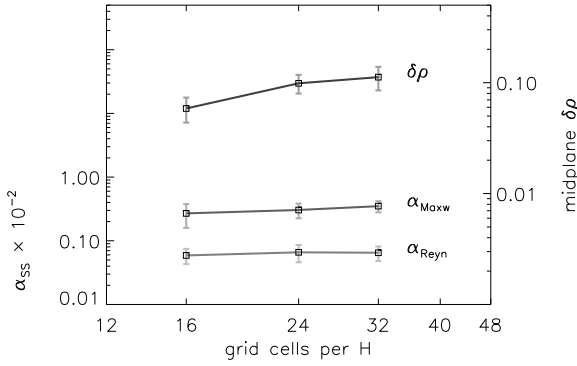


**Figure A1.** Dependence of key quantities on the numerical resolution. Error bars indicate fluctuations within the used time interval of  $t = 20 - 50$  orbits. All results presented in this work adopt a value of 24 grid cells per  $H$ .

- Sano T., Inutsuka S.-i., Turner N. J., Stone J. M., 2004, *ApJ*, 605, 321  
 Sano T., Miyama S. M., 1999, *ApJ*, 515, 776  
 Sano T., Miyama S. M., Umebayashi T., Nakano T., 2000, *ApJ*, 543, 486  
 Sano T., Stone J. M., 2002, *ApJ*, 577, 534  
 Sicilia-Aguilar A., Hartmann L. W., Briceño C., Muzerolle J., Calvet N., 2004, *AJ*, 128, 805  
 Sorathia K. A., Reynolds C. S., Armitage P. J., 2010, *ApJ*, 712, 1241  
 Stewart S. T., Leinhardt Z. M., 2009, *ApJ*, 691, L133  
 Turner N. J., Drake J. F., 2009, *ApJ*, 703, 2152  
 Turner N. J., Sano T., 2008, *ApJ*, 679, L131  
 Turner N. J., Sano T., Dziourkevitch N., 2007, *ApJ*, 659, 729  
 Umebayashi T., 1983, *Progress of Theoretical Physics*, 69, 480  
 Umebayashi T., Nakano T., 1981, *PASJ*, 33, 617  
 Umebayashi T., Nakano T., 2009, *ApJ*, 690, 69  
 Wardle M., 1999, *MNRAS*, 307, 849  
 Wardle M., 2007, *Ap&SS*, 311, 35  
 Wardle M., Salmeron R., 2011, *ArXiv e-prints*  
 Weidenschilling S. J., 2000, *Space Sci. Rev.*, 92, 295  
 Weidenschilling S. J., Cuzzi J. N., 1993, in E. H. Levy & J. I. Lunine ed., *Protostars and Planets III Formation of planetesimals in the solar nebula*. pp 1031–1060  
 Wetherill G. W., Stewart G. R., 1993, *Icarus*, 106, 190  
 Wyatt M. C., 2008, *ARA&A*, 46, 339  
 Yang C., Mac Low M., Menou K., 2009, *ApJ*, 707, 1233  
 Youdin A. N., Goodman J., 2005, *ApJ*, 620, 459  
 Ziegler U., 2004, *JCoPh*, 196, 393  
 Zsom A., Ormel C. W., Güttler C., Blum J., Dullemond C. P., 2010, *A&A*, 513, A57+

## APPENDIX A: NUMERICAL CONVERGENCE CHECK

To verify that our simulations are numerically converged, we performed two additional runs identical to model D1.1, but with the numerical resolution changed to 16, and 32 grid cells per  $H$ , respectively. Owing to constraints in computational cost, we were not able to evaluate gravitational torques for the higher-resolved run but have to rely on the hydrodynamic quantities as proxies instead. The dependence of key quantities defining the turbulent state of the fluid are shown in Figure A1.

As was briefly discussed in Sect. 4.2, the numerical require-

ments for resolving the development of the MRI in the presence of a net vertical field are safely established by linear theory. Accordingly, we see very little change in the turbulent stresses  $\alpha_{\text{Maxw}}$ , and  $\alpha_{\text{Reyn}}$  when increasing the numerical resolution beyond the basic requirement. However, from our study of the box-size dependence in Paper I, we recall that convergence in these quantities does not necessarily guarantee that secondary effects are equally well resolved. In particular, this applied to the convergence (with box size) in the amplitude  $\delta\rho$  of the excited of spiral density waves. Because of the predicted non-linear steepening of the analytic wave profile (Heinemann & Papaloizou 2011), we suspect that spurious numerical dissipation might have an influence on the lifetime of wave fronts and hence on the overall amplitude of density perturbations.

This effect is seen in the dependence of  $\delta\rho$  on the numerical resolution as shown by the upper line in Figure A1. There  $\delta\rho$  changes by almost 70% when increasing the number of points from 16 to 24 per  $H$ , i.e., for a 50% increase in linear resolution. In contrast, when going from 24 to 32 cells (corresponding to an additional 33% increase in resolution), the change in  $\delta\rho$  remains below 15%, such that the discrepancy between the two resolutions is consistent within the error bars. Put into proportion with the level of accuracy aimed for, this indicates that our standard resolution of  $24/H$  is reasonably converged and will allow to predict turbulent density fluctuations to within about  $\pm 25\%$ .

## APPENDIX B: MODIFICATIONS TO THE INDUCTION EQUATION

Let us first focus on the time step limitations imposed by the high value of the diffusivity coefficient  $\eta$  near the disc midplane (cf. Fig. 1). Given the need to evolve the simulations over several hundred dynamical time scales to follow the evolution of the embedded planetesimals, using these profiles is prohibitive. By inspecting earlier simulations and test runs, however, we have determined that there exists no significant small-scale structure in the regions of high diffusivity. This is hardly surprising as the diffusion term is very efficient at removing features in the magnetic field topology. We have found that imposing a cap to the diffusivity,  $\eta$ , corresponding to a value of  $\text{Rm} = 3$ , does not significantly change the observed field topology, while at the same time permitting a much larger computational time step. However, as we will see below, additional care has to be taken to make this approach viable.

### B1 Evolution of mean fields

Owing to the periodic nature of the shearing box approximation, the only field structures that remain in the dead zone region are vertical variations in the radial and azimuthal field. Magnetic fields are essentially uniform in the horizontal directions. The vertical variations are given by the horizontally-averaged mean values  $\bar{B}_x(z)$ , and  $\bar{B}_y(z)$ . Let us now examine how these are affected by diffusion. Note that the induction equation

$$\begin{aligned} \partial_t \mathbf{B} - \nabla \times (\mathbf{v} \times \mathbf{B} - \eta \nabla \times \mathbf{B}) &= 0, \\ \nabla \cdot \mathbf{B} &= 0, \end{aligned} \quad (\text{B1})$$

is linear in both  $\mathbf{B}$ , and  $\eta$ , and can be decomposed accordingly. For reasons that will become obvious in a moment, we split the induction equation into two parts, reflecting the evolution of the horizontally averaged mean fields and their fluctuations (cf. Gressel 2010). Because the geometric averaging operation trivially commutes with

the differential operators in (B1), this decomposition is exact. Focusing on the evolution of the mean fields, we now write down the diffusive part of the related induction equation:

$$\partial_t \bar{B}_i(z) = \dots + \partial_z \left[ \eta(z) \partial_z \bar{B}_i(z) \right], \quad i \in \{x, y\}. \quad (\text{B2})$$

Introducing a cap on the value of  $\eta$  (and hence removing its  $z$ -dependence beyond a certain depth within the dead zone) may significantly alter the character of (B2), and we illustrate this by means of a simple example: Note that for constant  $\eta$ , a field varying linearly with  $z$  is not subject to any further diffusion as  $\eta \partial_z^2 \bar{B}_i(z) = 0$  in this case. In contrast, any ‘‘bump’’ in  $\eta$  will make  $\eta(z) \partial_z \bar{B}_i(z)$  vary in  $z$  even if  $\partial_z \bar{B}_i(z)$  is constant. The diffusion term will then act to flatten a given linear ramp, removing any residual gradients in  $\bar{B}(z)$ . Looking at the strong gradients  $\partial_z \eta(z)$  seen in Fig. 1, this implies a potentially efficient means to redistribute field. Ultimately, a weak gradient in  $\bar{B}$  can lead to strong diffusion in the presence of a large gradient in  $\eta$ .

Because it is a one-dimensional equation, the overhead of solving (B2) is computationally inexpensive, even under stringent time step constraints. Consequently, we split (B1) into four parts by separating both  $\mathbf{B} = \bar{\mathbf{B}} + \mathbf{B}'$  and  $\eta = \eta_{>3}(\mathbf{x}, t) + \eta_{<3}(z, t)$ . Here subscripts refer to the resulting magnetic Reynolds number,  $Rm$ , as indicated by a dashed line in Fig. 1; also note the function arguments indicating that the highly diffusive low- $Rm$  part of  $\eta$ , (i.e.  $\eta_{<3}$ ) is only applied to the mean-field equation. In summary, this approach allows us to retain the full  $\eta$  profile in (B2), while using the capped  $\eta$  profile in the expensive three-dimensional equation. We finally remark that retaining the full  $\eta$  in the mean fields will likely enhance the leakage of field into the dead zone, as discussed above.

## B2 Accounting for super-box scale effects

Neglect of the large-scale radial structure makes the shearing-box a poor set-up for global magnetic field evolution. This deficiency becomes most apparent within the dead zone, as we have discussed briefly above. Accounting for the global disc topology, Turner & Sano (2008) derived a criterion for the evolution of large-scale magnetic fields within dead zones. Owing to the limitations imposed by the neglect of curvature terms, shearing boxes cannot reproduce the related threshold, which applies in global cylindrical coordinates. This is because the divergence of radial field lines is not included, so  $B_x$  can be uniform where  $B_r$  would decline as  $1/r$ . Omitting radial gradients in  $B_r$  contributes to the uniform shear-generated  $B_\phi$  and the weak resistive diffusion.

Moreover, in a global disc model, the Keplerian rotation profile  $\Omega(r) \propto r^{-3/2}$  leads to a radial variation of the shearing time scale. In contrast, a single orbital frequency  $\Omega_0$  applies throughout the local box, such that a uniform radial field stretches out into a uniform toroidal field. With the toroidal field uniform, the resistive term  $\eta \nabla^2 B_\phi$  in the induction equation toroidal component is zero, preventing the diffusion of the shear-generated fields. As a result, local simulations of dead zones can exhibit the growth of large toroidal flux (cf. Hirose & Turner 2011), which may spuriously feed-back into the MRI-active regions.

One possibility to account for the global field evolution would be to remove toroidal flux at a rate consistent with the solution of the global induction equation. For example, if one assumed a power-law radial dependence for the dead zone toroidal field  $B_\phi \propto r^p$ , and a radially uniform resistivity, the axisymmetric cylindrical induction equation has resistive term  $\partial_t B_\phi = \eta B_\phi (p^2 - 1) r^{-2}$ . Because of the uncertainty related to the parameter  $p$ , we chose an

even simpler approach and estimate the time scale on which diffusion redistributes azimuthal flux as

$$\tau_{\text{diff}} = \frac{1}{k_r^2 \eta}, \quad \text{where we chose } k_r \equiv \pi/r. \quad (\text{B3})$$

Noting that a Fourier mode of wave number  $k_r$  would exponentially decay according to  $\exp(-t/\tau_{\text{diff}})$ , we remove toroidal (and radial) flux via an additional source term

$$\partial_t \bar{B}_i(z) = \dots - \bar{B}_i(z)/\tau_{\text{diff}} \quad (\text{B4})$$

in the one-dimensional part of the induction equation. As we will find when discussing the results, this choice of the global decay time scale retains some weak fields within the midplane (also cf. fig. 3 in Hirose & Turner 2011), indicating that we are not significantly over-damping the system. As can be seen in the upper panel of fig. 5 of Paper II, model D1 is affected by relatively strong fields diffusing into the midplane region. To make the comparison with models D1.2, and D1.4 as straight-forward as possible, we decided to re-run this simulation including the diffusive sink term in Eqn. (B4), giving the new version the label ‘D1.1’.

This paper has been typeset from a  $\text{\TeX}/\text{\LaTeX}$  file prepared by the author.